Master Thesis

Implementation of an Ion Microscope with Differential Evolution Based Autofocus

Lina Hedewig

September 9, 2022

Supervisors: Dr. Boris Bergues, Prof. Dr. Matthias Kling

Thesis submitted to:

Ludwig-Maximilians-Universität München,
Fakultät für Physik

Masterarbeit

Implementierung eines Ionenmikroskops mit einem Autofokus basierend auf differentieller Evolution

Lina Hedewig

9. September 2022

Betreuer: Dr. Boris Bergues, Prof. Dr. Matthias Kling

Arbeit angefertigt an der

Ludwig-Maximilians-Universität München,
Fakultät für Physik

Contents

1.
Introduction

Resolving the motion of electrons in atoms and molecules on the shortest time scales is a key question addressed by attosecond science. A main task is to investigate and control the dynamics of the interaction between light and matter [1, 2]. As one of the basic and at the same time one of the fastest processes of light-matter interaction, photoionization by the means of intense laser pulses plays an important role in this field of physics. Several types of devices exist to investigate this process. Typically those instruments can discriminate between different ionic species, but cannot resolve their position within the field of view (FOV) where the respective ions were generated. However, the intensity distribution of a focused laser beam is rarely homogeneous but typically follows a Gaussian function. To allocate generated ions to specific intensities, it is crucial to know their birth positions.

Different approaches have been proposed to overcome this challenge [3–5]. Ion microscopy is one of those approaches and was introduced in 2011 [6]. It combines the ionic species resolution by a time-of-flight detector with imaging features leading to spatial resolution. Due to the visual access to the interaction region, an ion microscope (IM) cannot only be used to investigate ionization processes, but also serve for laser focus diagnostics. One of the advantages of an IM in this case is that the laser doesn't have to be blocked for the analysis e.g. with a camera, but the very same beam analyzed with the IM can be directly used for further experiments. [7, 8]

Most of the IMs existing to date, though, are quite sensitive to deviations in the beam position or the voltages applied to the device's electrodes. For this reason, operating an IM oftentimes requires a time-demanding manual optimization of the voltages. Our approach is the implementation of a Differential Evolution (DE) based algorithm, which automatically determines the correct voltages for obtaining a sharp image. We call this an "autofocus" for the IM.

The automatic determination of the correct parameters now enables us to introduce additional electrodes. In manual operation it would be impossible to control an even larger amount of parameters, but not so with an autofocus. The

purpose of introducing additional electrodes is the aim of overcoming another challenge of ion microscopy: Typically, IMs are designed for one specific magnification only, based on the position of the constituent electrodes. Introducing additional electrodes allows for a higher flexibility of the device with respect to its magnification without loss of resolution. This leads us to present a novel, more generic IM design than current models. [9]

The goal of the present thesis is twofold: On the one hand, we want to make use of an IM to investigate the generation of doubly charged argon ions via the strong field ionization of singly charged argon. On the other hand, the auto-focusing generic IM mentioned above shall be simulated and implemented.

The thesis begins with an introduction to ion microscopy. The text following this first section is divided into two main parts according to the two goals.

The first part presents the experiment investigating the generation of doubly charged argon ions. We are interested in the question whether the generation of doubly charged argon is more efficient when starting from the first ionization state of argon or when starting from the ground state, making use of the effect of non-sequential double ionization (NSDI). To this end, there is a short introduction to NSDI, followed by the experimental concept and setup. After that, the obtained results are presented and discussed.

The second part treats the simulation and implementation of the novel generic IM design including an autofocus. The IM setup is presented and the DE algorithm used for the control of the device is introduced. Afterwards, simulations are presented investigating the device's performance with respect to different parameters, such as the number of electrodes involved in the optimization, the performance at different magnifications, the influence of imprecise focus positioning and the influence of fluctuations of the voltages applied to the electrodes. In the subsequent section follows a presentation of a test of the feasibility of our auto-focusing algorithm, using an existing IM. Finally, the steps taken towards the realization of the novel generic IM are presented.

2.
Ion Microscopy

The basic idea of ion microscopy is in principle similar to optical microscopy: An object is imaged by a lens to create an intermediate image, which is then imaged again by a second lens onto a detector. Both lenses magnify the image.

The object in case of ion microscopy are ions or, to be precise, ion distributions. Instead of optical lenses, electrostatic lenses are used to image ions in a very similar way to photons, creating ion paths comparable to optical rays. The detector typically consists of a Microchannel Plate (MCP) for signal amplification, followed by a phosphor screen and a CCD camera. But in principle any other spatially resolved ion detection system can be used as well.

There are several different kinds of electrostatic lenses serving different purposes like for example two- or three-element lenses, which might also be longitudinally asymmetric or quadrupole lenses. The most common type of lens is a three-element lens operated in einzel mode, corresponding to the optical bi-convex lens.

Such a lens consists of three annular or cylindrical electrodes. In einzel mode, the voltages applied to the first and last electrode are the same ($V_1 = V_3$) while the central electrode lies on a different potential ($V_1 \neq V_2 \neq V_3$). The sharp potential difference between the electrodes leads to the deflection of ions or electrons passing through the electrodes' center, analogous to the refraction of light at interfaces of materials with different refractive index. This kind of lens is called an einzel lens. [10]

The object to be observed is an ion distribution generated by a laser beam focused on gas atoms between two electrodes, the repeller and the extractor, which extract the ions from the interaction region. A schematic overview is depicted in figure 2.1. In the following thesis we will always refer to the IM's principal axis as the x axis, while the laser propagation direction is along the y axis.

For the kind of IM used during the experiments of section 3, there are two

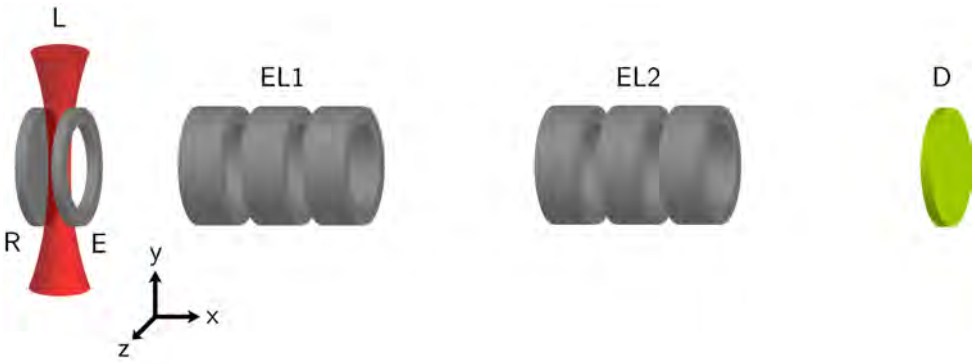

Figure 2.1: *Example of an IM setup. R: Repeller, E: Extractor, L: Laser, EL1/2: Einzel lens 1/2, D: Detector*

different modes of operation: the time of flight (TOF) mode and the imaging mode. In the imaging mode one has the additional option to gate the detector. The two modes can in principle be applied to all IMs with an MCP as part of the detector.

The TOF mode makes use of the fact that different ionic species with different mass over charge ratios $\frac{m}{q}$ have different times of flight through the device. The relation between arrival time at the detector t and specific charge $\frac{m}{q}$ is:

$$t \propto \sqrt{\frac{m}{q}}, \tag{2.1}$$

which is a consequence of the requirement that the particle's electrical potential energy is completely converted to kinetic energy E_{kin} at the detector. At the beginning of its flight, the ion's electrical potential energy is $q\,\Delta V$ due to the potential difference ΔV between the starting point and the detector. The requirement of energy conversation relates to:

$$q\,\Delta V = E_{kin}. \tag{2.2}$$

Assuming the simplified case of an ideal plate capacitor, the acceleration is constant and after plugging in the respective terms for the kinetic energy and velocity, one obtains formula 2.1.

Provided the voltages applied to the electrodes are properly set to obtain an image on the detector, the ions of the focal region impinge on the MCP and create an avalanche of secondary electrons.

When capacitively picking up the phosphor screen's voltage and providing this voltage to an oscilloscope, the signal gives the ion yield versus arrival time.

This has its origin in the fact that the arrival of an electron avalanche reduces the voltage for a short time before the voltage decreases back to its previous level. The oscilloscope has to be triggered to the laser repetition rate, for example by a photodiode detecting stray light.

The common way to operate an IM is in the imaging mode. The electrons leaving the MCP on its back side hit the phosphor screen and the resulting flash of light is detected by a CCD camera. The camera's output is an image of the ion distribution within the FOV.

The advantage of the ionic species resolution obtained from TOF can be transferred to the imaging mode by gating the MCP. To this end, one determines the arrival time of the ionic species to be investigated via the TOF mode. Afterwards, a gating pulse is provided to the MCP side facing the phosphor instead of the constant voltages in ungated mode. The MCP front side is always grounded. To be precise, the MCP back side voltage is not completely switched off while the gating pulse is off but set to a base voltage higher than zero, but low enough that no image is produced. The gating pulse adds some additional voltage, increasing the MCP back side voltage above the threshold needed for a sufficiently high number of electrons to be created to generate an image. When providing the gating pulse at the same time as the arrival time of ionic species of interest, the camera records an image of the ions of interest only. For a satisfactory ionic resolution, this requires the differences in time of flight to be larger than the duration of the gating pulse. Typical durations for the gating pulse are 10 ns.

3.
An Application of Ion Microscopy: Generation of Ar^{2+} via Strong-Field Ionization of Ar^{+}

IMs are used in several different kinds of experiments, like in focus diagnostics or studies of the ionization processes in atoms and molecules [7, 8, 11, 12].

In the present work, we use an IM for studying the ionization properties of argon. More precisely, we want to investigate whether the generation of Ar^{2+} is under certain conditions more effective when starting from the atomic ground state of argon than when beginning from singly charged argon ions in their ground state as initial state. This counterintuitive hypothesis is based on the idea that the process of non-sequential double ionization, which is to be explained in the following, might facilitate the direct transition from Ar to Ar^{2+} to such an extent that the process starting from Ar^{+} is less probable in comparison.

After an introduction to NSDI, the experimental concept, setup and results are presented and discussed.

3.1 Introduction to Non-Sequential Double Ionization

In 1982, L'Huillier et al. [13] observed a remarkable knee structure in the intensity dependence of the yield of laser-generated doubly charged noble gas ions similar to figure 3.1. The yield rises at intensities significantly lower than predicted by the sequential ionization model, which assumes that the electrons are liberated one after another and independently of each other via strong field ionization. [14, 15]

The subsequently developed model of non-sequential double ionization, on the other hand, accounts for the interaction of the two electrons. Though the details of the process are still the subject of active research, the most accepted explanation for this phenomenon is the simple man's model. A visualization of the process is given in figure 3.2.

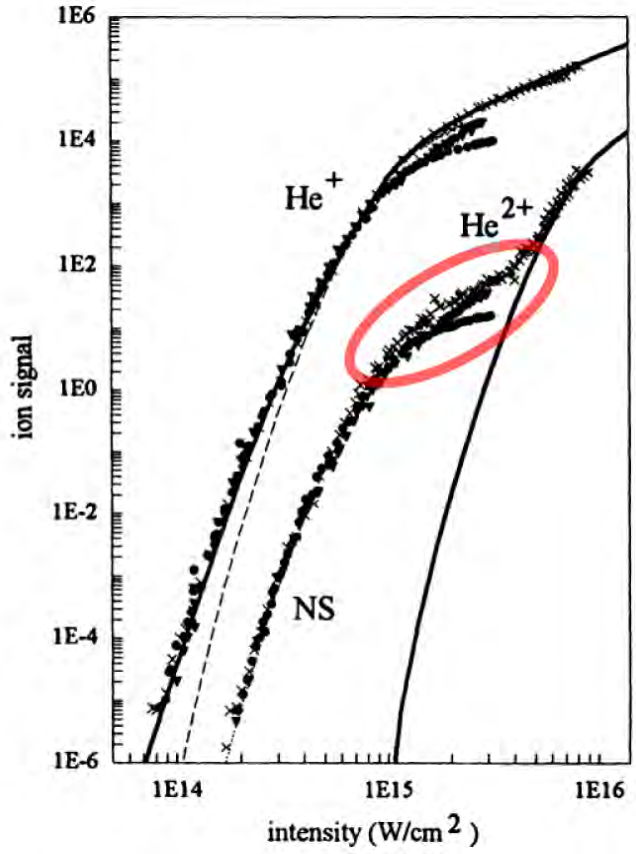

Figure 3.1: *Typical knee structure in the intensity dependence of twofold charged ion generation. For He^{2+}, the solid line marks the theoretical results expected for sequential ionization. NS denotes the non-sequential regime. On top of the original image, the knee is pronounced in red. Adapted from Walker et al. [16].*

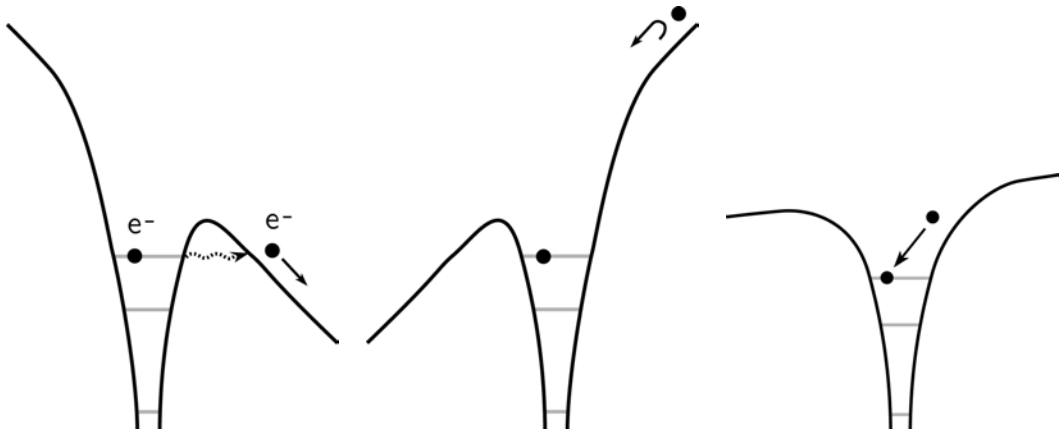

Figure 3.2: *Visualization of the behavior of the atomic potential in a strong laser field and the two electrons moving in it according to the simple man model. The three steps consist of the tunneling ionization (a), the free propagation of the primary electron and acceleration back to the parental ion (b) and the recollision of the primary electron with the ion, liberating a second electron (c).*

According to the model, the strong laser field first bends the atomic potential. Near the maximum of the field, an electron has the highest probability to tunnel through the resulting potential barrier. The atom is tunnel ionized, which is a quantum process. Afterwards, the electron is accelerated by the laser field presumably independent of the ion's potential and, when the linearly polarized field changes its sign, driven back towards its parental ion. This movement is treated classically. With some probability depending on the instant of the release, the electron may re-collide inelastically with the parental ion and thereby "kick out" a second electron. Due to the mixture of quantum and classical treatment of the movement, the model is also known as the semi-classical recollision model.

The point in time when the primary electron is emitted determines the kinetic energy with which it returns to the parental ion. Electrons emitted before the field maximum do not return to the ion once they left its direct vicinity but are driven away from their core. If the primary electron is emitted exactly at the field maximum, it returns with zero kinetic energy. Only electrons emitted after the field maximum return with finite kinetic energy and are able to liberate a second electron. [17, chapter 7]

Beyond the saturation intensity of the singly charged ion, the sequential double ionization process becomes increasingly likely, the higher the intensity. The chance that the singly charged ion becomes further ionized via the absorption

of a sufficiently high number of photons increases more strongly than the probability of a recollision process liberating a second electron. The characteristic knee structure in the doubly charged ion yield's intensity dependence marks the transition from one ionization process to the other. [12, 14, 15]

3.2 Experimental Concept

The aim of the experiment presented in this chapter is to find out which of the two following processes is more efficient for the generation of doubly charged argon ions by an infrared (IR) beam: The IR photoionization of singly charged argon ions in their ground state or the NSDI starting from neutral argon as initial state.

Previously it has been shown that ions can behave differently from their neutral partners. For example, the production of triply-charged argon ions is strongly suppressed when Ar^+ instead of Ar is used as initial target [18]. Our hypothesis is that the rescattering of the first electron in the NSDI process facilitates the ionization process to such an extend that the NSDI ionizing Ar directly to Ar^{2+} is more efficient than the ionization of Ar^+ to Ar^{2+}.

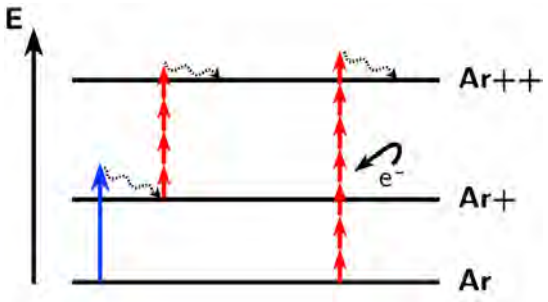

Figure 3.3: *The two excitation schemes to be compared. Energy deposition by an XUV photon is qualitatively depicted by a blue arrow, IR photons by red arrows. The excess energy is carried away by the ejected electron, which is denoted by a dashed arrow. The path on the right-hand side is the non-sequential double ionization.*

Previous experiments have already treated similar questions. However, the typical preparation process cannot prevent excited ion states to be generated. As a consequence, the initial state is not clearly defined. [18] Our idea is to prepare the singly charged argon ions by an extreme ultraviolet (XUV) pulse. If the spectrum of the pulse is chosen correctly, one can precisely generate just the one state of interest, in our case Ar^+ in its ground state. Hence, our experimental concept is based on a pump probe scheme with an XUV and an IR

pulse. The two pulses have some delay in between them so that the XUV pulse can be sent in first to prepare the singly charged argon ions. The consecutive IR pulse is supposed to further ionize the gas to Ar^{2+}. This is to be compared with the Ar^{2+} yield when only the IR beam is switched on.

To access the two excitation paths of interest, we use a laser source delivering a pulsed IR beam centered at 800 nm and a pulsed XUV beam consisting of the high harmonics up to the 21st harmonic of the fundamental IR beam. First, we determine the Ar^{2+} yield generated by the IR beam only. In principle, there are two excitation paths for this case as shown in figure 3.4a: the non-sequential double ionization (left-hand side) and the sequential ionization pathway via the ionic ground state (right-hand side). If the power is set appropriately in the power regime where NSDI is preferred, one may assume the sequential ionization negligible. The second setting to be compared with the first is with both IR and XUV beam, and a delay between them so that the XUV pulses run ahead of the IR pulses. The resulting ionization pathways are depicted in figure 3.4b. The power of the IR is untouched so that the IR sequential double ionization is still suppressed. The pulse energy of the XUV has to be high enough to ionize a significant portion of the argon atoms to Ar^{+}. At the same time the XUV intensity has to be low enough that two-XUV-photon processes are negligible. The experimental procedure to reach the desired settings is explained in section 3.4.

When the mentioned parameters are properly set, the only two excitation pathways remaining are those of interest. In the IR-only case, all Ar^{2+} are generated via NSDI. When the XUV is switched on, a portion of the Ar^{2+} yield will be generated via the sequential XUV+IR process. A decrease of the total Ar^{2+} yield after irradiation with the XUV pulse would indicate that the strong field ionization of Ar^{+} from the ionic ground state is less probable than the NSDI of Ar.

3.3 Setup

The laser system used for this experiment is based in Heraklion, Greece, at the Foundation of Research and Technology - Hellas (FORTH). On overview of the setup is given in figure 3.5. It operates with a central wavelength of 800 nm, a pulse duration of 25 fs and a repetition rate of 10 Hz. Via high harmonic generation (HHG) in a xenon gas jet, XUV radiation in the form of an attosecond pulse train of 10 fs duration can be generated featuring harmonics up to the 21st, corresponding to a photon energy of up to 32.5 eV. [19, 20].

To introduce timing differences between the IR and XUV pulses, we employ a delay plate setup as shown in figure 3.6. The IR beam passes through a

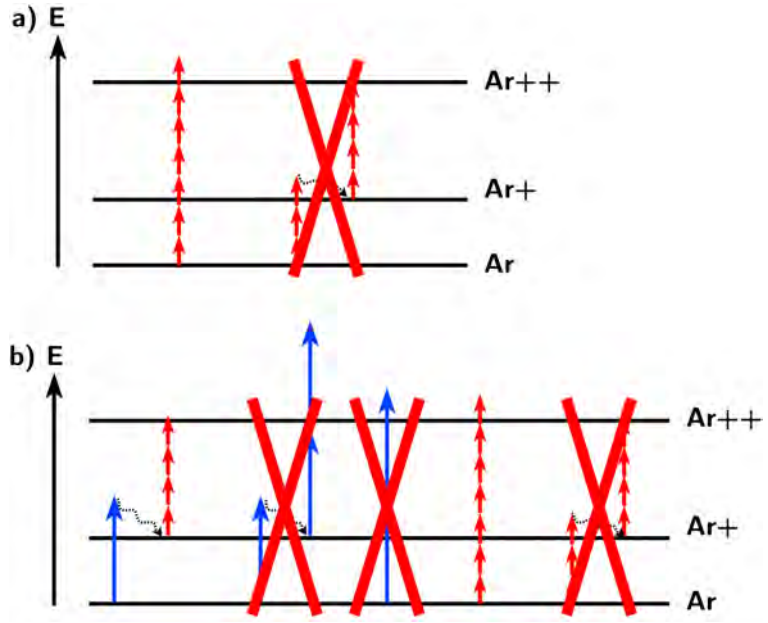

Figure 3.4: *The experimentally accessible excitation schemes to be compared. a) With IR only, sequential ionization is suppressed by proper power setting. b) With XUV and a delayed IR, two-XUV-photon processes are suppressed by proper intensity setting.*

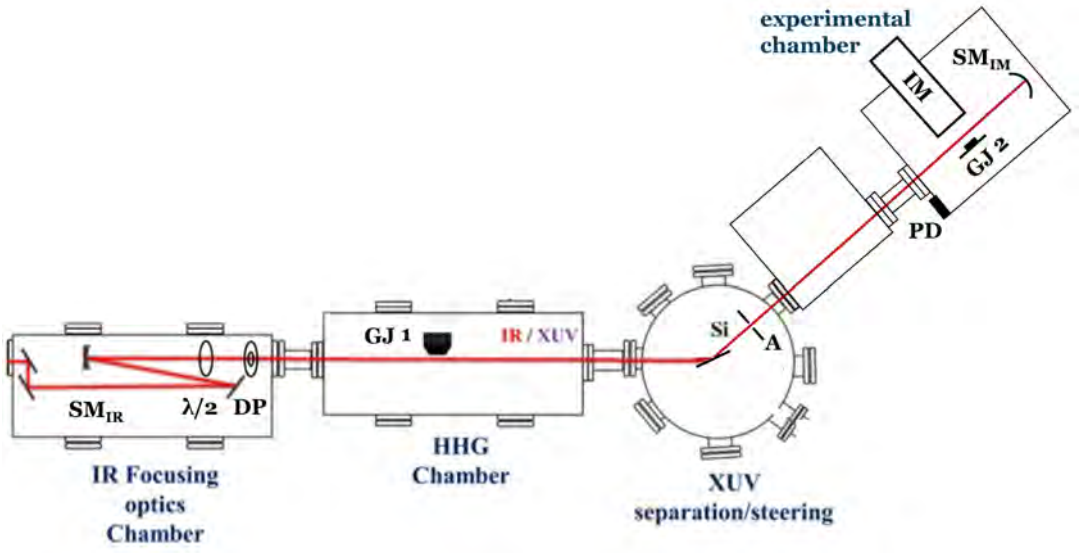

Figure 3.5: *Optical layout of the setup. SM_{IR}: spherical mirror of* 9 m *focal length,* $\lambda/2$*: half-wave plate, DP: delay plates, GJ1: pulsed xenon jet, Si: silicon plate, A: aperture, SM_{IM}: gold coated spherical mirror of* 15 cm *focal length, GJ2: Ar gas jet, IM: Ion microscope, PD: photodiode. Adapted from Nayak et al. [19].*

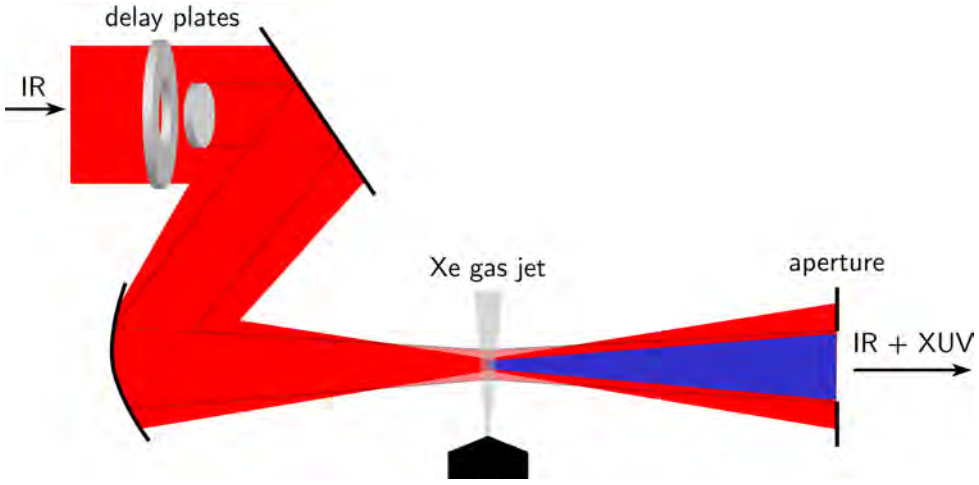

Figure 3.6: *Working principle of the delay line. The inner delay plate can be tilted with respect to the outer plate.*

radially split glass plate where the inner part can be tilted with respect to the outer part. Due to its larger diameter, the outer part of the beam will be focused more strongly by the consecutive focal mirror and generates the XUV pulses in the HHG process. An iris behind the HHG region blocks the annular outer part of the IR laser while the generated XUV pulse passes through the aperture due to its smaller divergence originating from its shorter wavelength [21, Chapter 4] together with the inner IR pulse.

The delay introduced by the plates is estimated by the following calculation to be on the order of 1 ps for the case of the XUV coming before the IR. Both the inner and outer plate are about $d = 3\,\text{mm}$ thick fused silica. To have the possibility to set both positive and negative delays of the inner beam relative to the outer beam, the outer plate is mounted with a tilt of about 10° with respect to the laser propagation direction while the inner plate can be rotated in a range of $[0°, 25°]$. The time delay t introduced by one of the glass plates depends on the respective rotation angle α and can be determined with the following equation:

$$t(\alpha) = \frac{\textit{effective glass thickness}}{\textit{group velocity}} = \frac{d \cdot n_{group}}{\cos\alpha \cdot c}. \tag{3.1}$$

For the IR wavelength of 800 nm, the group refractive index n_{group} evaluates to 1.4671 [22]. As a consequence, the delay differences introduced for the XUV-first experiments are in the range of $t(20°) - t(10°) = 710\,\text{fs}$ to $t(25°) - t(10°) = 1290\,\text{fs}$. When setting IR first, the delay is about $t(10°) - t(0°) = 230\,\text{fs}$. Even though the exact delay cannot be assessed due to imprecise angle control, the delay is definitely larger than the pulse's intensity full width at half maximum (FWHM) of 25 fs. This still holds true if one includes an estimated angle uncertainty of 3°, which results in a minimum delay of 90 fs in the case of IR-first.

After passing through the aperture, the reflection from a silicon plate placed close to Brewster's angle for the IR significantly reduces the IR intensity. Based on the refractive index for silicon of $n_{Si}(800\,\text{nm}) = 3.6941$ [22], the Brewser's angle evaluates to $\theta_B = \arctan\frac{n_{Si}(800\,\text{nm})}{n_{vacuum}} = 74.8°$. The $\frac{\lambda}{2}$-wave plate has been rotated by about 10° relative to the position of minimum IR reflection. Hence, with the use of the Fresnel equations, one obtains a reflected intensity of about 2.2% of the original intensity. [21]

If only the IR beam is desired during experiment, one can simply switch off the xenon gas jet for HHG.

In the experimental chamber, the two collinear beams impinge on a back reflecting gold mirror of focal length 5 cm and are focused between the repeller and the extractor of an IM (IMT12 by the Stefan Käsdorf GmbH [23]). Figure 3.7 schematically shows the IM's setup where two einzel lenses image the ions

onto an MCP followed by a phosphor screen. The pressure in the experimental chamber was $1.1 \cdot 10^{-5}$ mbar, in the tube of the IM containing the electrodes it was slightly higher with $6.1 \cdot 10^{-6}$ mbar. A pulsed gas argon jet emitted along the x-axis of the IM from a rectangular nozzle of dimensions $y = 3.3$ mm and $z = 0.5$ mm serves as target. It is triggered by a photodiode detecting diffusely backscattered light of the laser.

A more detailed description of the beamline, especially regarding the XUV generation, can be found in Makos et al. [20].

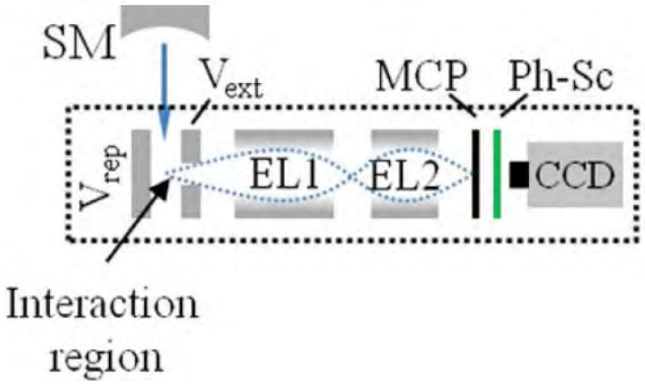

Figure 3.7: *A sketch of the IM. EL1/EL2: Einzel lens 1/2, MCP: Microchannel plate, Ph-Sc: Phosphor screen, CCD: CCD camera, SM: Spherical Mirror, V_{rep}: Electrode with ion repelling voltage and gas jet, V_{ext}: Electrode with ion extracting voltage. Adapted from Tsatrafyllis et al. [24]*

3.4 Execution of Experiment

The first step to be accomplished is setting the correct power of the IR beam to be below the knee in Ar^{2+} yield. For this reason we switch on the IR beam only and set the IM to TOF mode. A typical resulting oscilloscope image is shown in figure 3.8.

Next, the power of the IR pulses is varied and the argon ion yields are monitored. This results in the plot of figure 3.9. The knee structure is observed in the Ar^{2+} curve, which reveals that energies in the range of 40 mJ to 75 mJ lie in the regime where non-sequential double ionization is preferred. The flattening of the Ar^{2+} yield is not due to the onset of saturation since for one thing, the slope increases again for energies higher than 130 mJ, although the small amount of datapoints above the knee make it difficult to assess this. Additionally, the onset of the knee takes place when the yield of Ar^{+} begins to saturate, as the

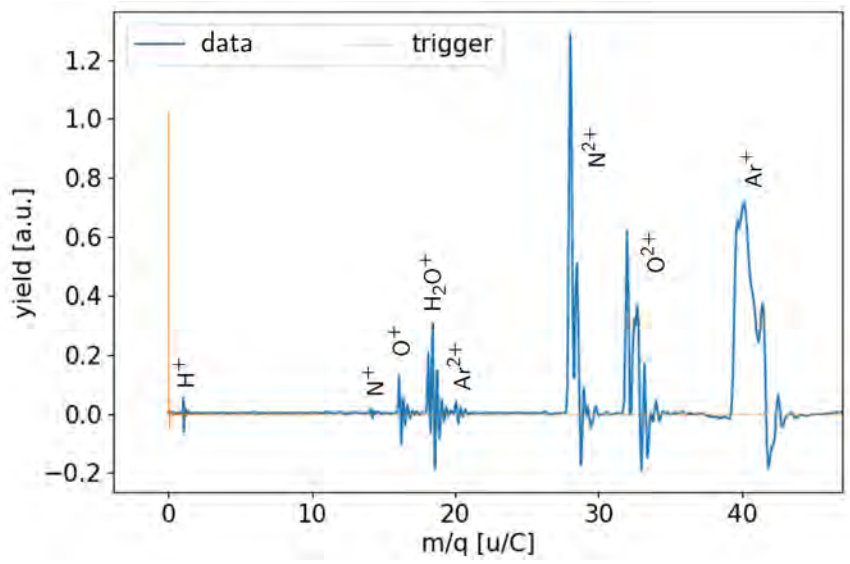

Figure 3.8: *A typical TOF spectrum recording the different ionic species at different arrival times according to their mass over charge ratio.*

sequential process of Ar^{2+} generation sets in only when the Ar^{+} generation is saturated. [12, 13, 16, 25]. This is something we could also confirm for measurements of other days with a more pronounced knee.

Since the XUV generation needs the full IR power, but for the experiment we want to reduce the power below the knee, instead of tuning the laser power, we make use of the $\frac{\lambda}{2}$-wave plate. By turning the wave plate, the IR power at the HHG region is not influenced, only the polarization. At the silicon plate placed close to Brewster's angle for the IR, however, the reflected power strongly depends on the laser polarization, which allows us to adjust the power delivered to the experimental chamber. As the dependence of reflected power on the laser polarization is highly nonlinear and determining the power from this would be challenging, a photodiode recording diffusely scattered IR laser light serves as a power reference in the experimental chamber. After setting the incoming IR power back to its maximum value, we adjust the wave plate until the estimated pulse energy is 50 mJ, based on the photodiode output value. This value is bookmarked to be used for the later experiments.

To determine the correct settings for the XUV pulses, we rotate the $\frac{\lambda}{2}$-wave plate so that no detectable signal is left in the TOF signal. Meanwhile, the xenon jet for XUV generation is still switched off. This process ensures that when now switching on the XUV, all we record is generated exclusively by XUV. Adjusting the XUV intensity is done by adjusting the delay of the xenon gas jet for HHG. The shorter the delay between the gas release and the arrival of the IR

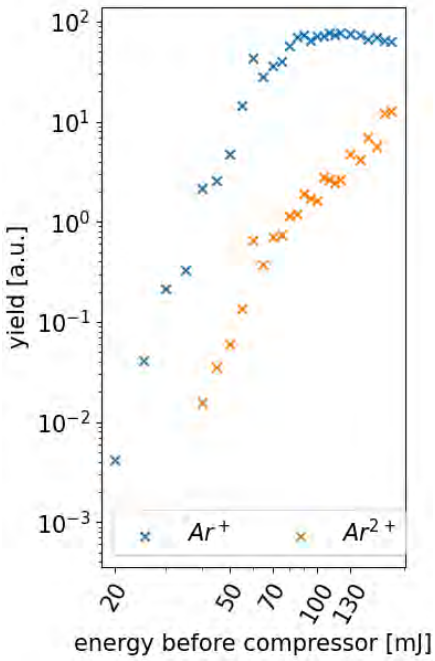

Figure 3.9: *Ar^+ and Ar^{2+} yield as a function of the energy of the IR beam indicating the knee in Ar^{2+} between* 75 mJ *and* 130 mJ.

laser pulse, the denser is the gas at the moment of the pulse's impact. And the denser the gas for HHG, the higher the XUV intensity. In this XUV-only setting we observe the Ar^{2+} signal and adjust the XUV intensity until no recordable Ar^{2+} signal is left. By this procedure we can exclude that two-XUV-photon processes play a notable role while keeping the pulse energy as high as possible to have a high number of one-XUV-photon absorptions.

Once the correct experimental conditions are determined, we switch the IM to imaging mode with the trigger fixed at the previously determined TOF of Ar^{2+} ions. A difficulty regarding the gating of the IM is the background of H_2O^+ ions. The signal generated by this ionic species is typically stronger than the Ar^{2+} peak and the temporal separation of the two peaks is about the same size as the gating pulse duration. A background image is obtained by recording an image with the same conditions as for the measurements but with blocked laser beam. Figure 3.10 shows a typical resulting image after subtracting the background and rotating the image so that the laser propagation direction is horizontal.

After these preparations, the actual measurement can be conducted. Using the delay plates, three delays are set, enabling us to record the ion yield for IR only, IR followed by XUV and XUV followed by IR.

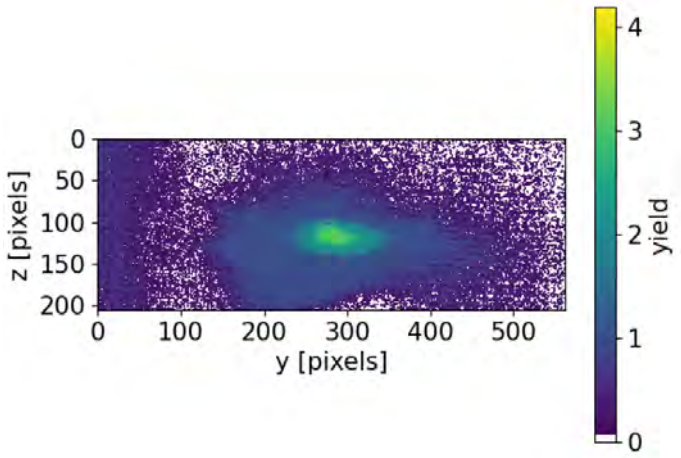

Figure 3.10: *IM image of Ar^{2+}. The increase in signal on the left-hand side is probably generated by H_2O^+.*

3.5 Results and Discussion

The resulting yields integrated along the direction perpendicular to the laser propagation direction are put together in figure 3.11. Each curve is averaged over four consecutive measurements.

It is apparent that these measurements contradict our expectation that the Ar^{2+} yield for XUV-first should be lower than for IR-only. Rather, we observe the opposite. Namely, there is a strong increase when switching on the XUV. This has been observed on several days and is reproducible. A possible explanation will be discussed further below.

Also, the case of IR-first results in a significantly higher Ar^{2+} yield than IR-only. Herein we don't see anything unexpected. The amount of Ar^{2+} ions generated by the IR pulse will be the same as in the case of IR-only and the XUV photon energy is not high enough to ionize Ar^{2+} to Ar^{3+} with one single photon, which would be the only way to reduce the Ar^{2+} yield with the XUV. This process would require a photon energy of at least 40.7 eV [26]. Hence, the only difference is that the XUV pulse following the IR pulse can further ionize the Ar^+ ions generated by the IR to Ar^{2+}.

Consistent with the XUV power calibration, the measured yield for XUV-only has no recordable signal. Hereby it is confirmed once again that our XUV power is low enough and that the high yields of XUV-first and IR-first arise only due to the interplay of IR and XUV.

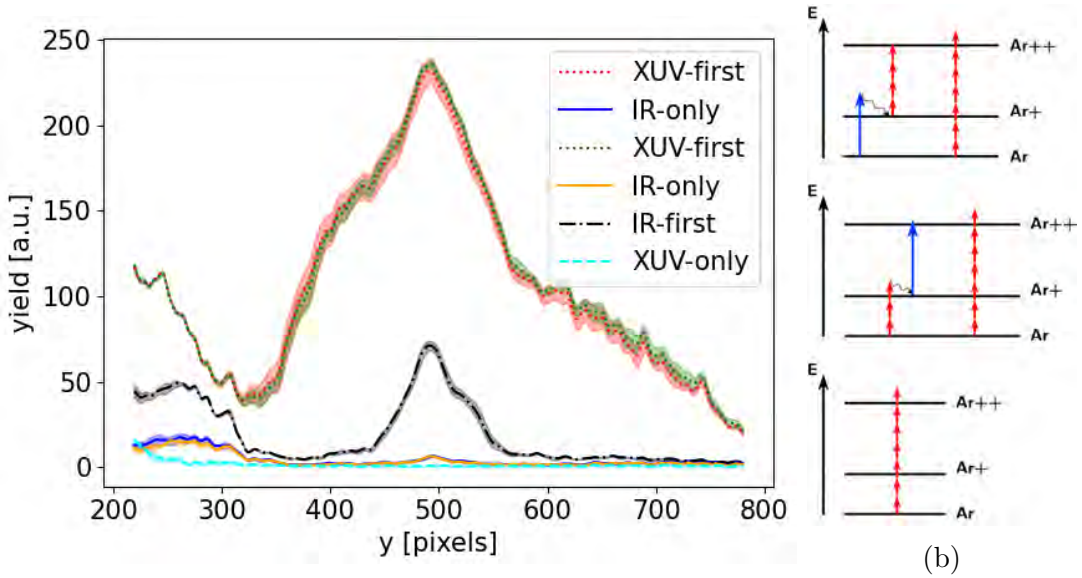

(a) (b)

Figure 3.11: *a) Ar^{2+} yields on the IM integrated along the z axis for different settings. The labels "XUV-first" and "IR-first" appear twice since the respective measurement was conducted twice to demonstrate reproducibility. The order of labels is the order in which the measurements were conducted. b) Reminder of the corresponding expected ionization processes for XUV-first, IR-first and IR-only from top to bottom.*

The most reasonable explanation for our unexpected results regarding XUV-first is to be found in the XUV spectrum. In fact, as we did not put any filtering elements into the beam path to avoid blocking the IR beam, we have to consider the full harmonic spectrum, not only the highest harmonics.

The first question to be addressed is whether some harmonics may excite resonant states of the argon atom, i.e. that they might excite the atom without ionizing it. Unfortunately, no XUV spectrum determining all harmonics and their respective intensities is directly available for this laser system. An estimation of the spectrum can be obtained by the analysis of spectra measured with different filters and dividing by the filter transmissions. Nevertheless, this only results in a very rough estimate, as becomes clear when following the extraction process performed in appendix 7.1. The resulting spectrum is shown in figure 3.12.

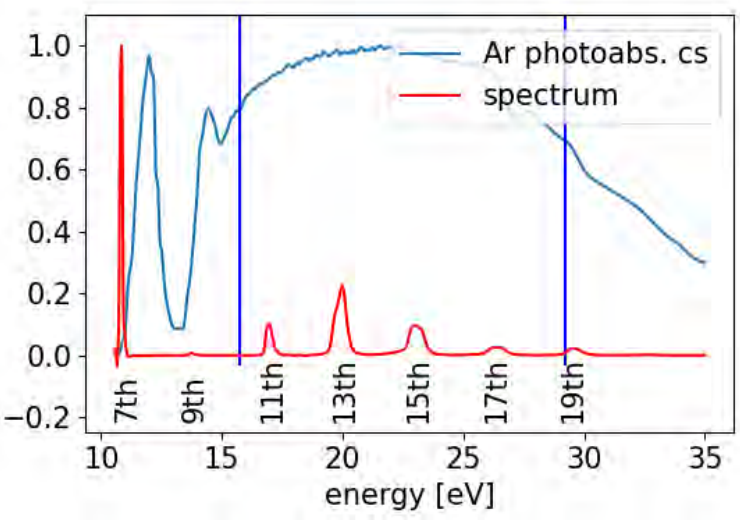

Figure 3.12: *Ar photoabsorption cross sections based on data by Chan et al. [27] and extrapolated XUV spectrum, both normalized. The left perpendicular line marks the ionization threshold of Ar, the right line denotes the first excitation state of* Ar^+.

In combination with the photoexcitation cross section of argon obtained by Chan et al. [27] it becomes apparent that while the harmonics 11 to 19 lie above the argon's ionization threshold of 15.8 eV [26], the presence of the 7^{th} and 9^{th} harmonics will excite some of the argon atoms without ionizing them. This adds another ionization pathway towards Ar^{2+} to our scheme, namely the excitation of Ar by the XUV, followed by an NSDI caused by the IR. It is obvious that this process is more favorable than a pure NSDI by IR only, since the facilitating

effect of the re-scattering will still be present, while the liberation of the first electron is facilitated by the excitation due to the XUV. However, according to the extrapolated spectrum, the 9^{th} harmonic is very weak and will most likely not lead to any notable contribution. The 7^{th} harmonic, even though significantly stronger, does not coincide with the argon resonances. Only the wings of this harmonic will contribute to an excitation of argon.

When multiplying the obtained spectrum with the photoabsorption cross section, one can compare the number of absorbed photons below and above the ionization threshold, corresponding to the number of generated excited argon states and the number of generated Ar^+ ions, respectively. The resulting ratio evaluates to $\frac{exited\ atoms}{ionized\ atoms} = 0.016$. As a consequence, for the ionization process with the step via excited argon to significantly alter the Ar^{2+} yield, this process of NSDI of excited argon has to be about 62.5 times stronger than the process of single ionization via the XUV towards Ar^+, followed by the ionization towards Ar^{2+} by the IR pulse.
Additionally to be considered are the lower harmonics up to the 7^{th} harmonic. For this spectral range, unfortunately, there are no data available for the specific laser system used for this experiment. The harmonic intensity is expected to rise exponentially with decreasing harmonic order as soon as they enter the perturbative regime, as long as the necessary phase matching conditions are met. For HHG on xenon, however, the perturbative regime is limited to the 3^{rd} harmonic [17, chapter 10].

In case the low harmonics are intense enough to trigger two-photon processes, there are several combinations which would result in an energy in the resonance region of argon, namely HH1 + HH7 = HH3 + HH5 = 12.4 eV, which falls into the right wing of argon's first resonance and HH1 + HH9 = HH3 + HH7 = HH5 + HH5 = 15.5 eV $<$ 15.8 eV , which is right below but still less than the ionization threshold. Thus, it may excite some of the argon's Rydberg states. A more detailed analysis of the influence of lower harmonics would require a spectrum of the harmonic intensities for this specific setup.

Additionally, there are also a small amount of excited argon ions generated. As can be seen from figure 3.12, the 19^{th} harmonic is slightly above the singly ionized argon ion's excitation energy of 29.2 eV. Assuming every absorbed photon above the excitation threshold generates an excited argon ion, the ratio between argon ions in their ground state to excited argon ions is 24.4. Hence, for the path via excited argon states to significantly contribute to the Ar^{2+} yield it has to be about 24 times stronger than the process of interest. This adds another point of uncertainty to the analysis.

The only conclusion we can draw at this point is that the recorded results are not as expected, but the fact that the XUV spectrum, in principle, allows

for additional excitation paths may provide an explanation for our observations.

A summary of all possible excitation paths is presented schematically in figure 3.13.

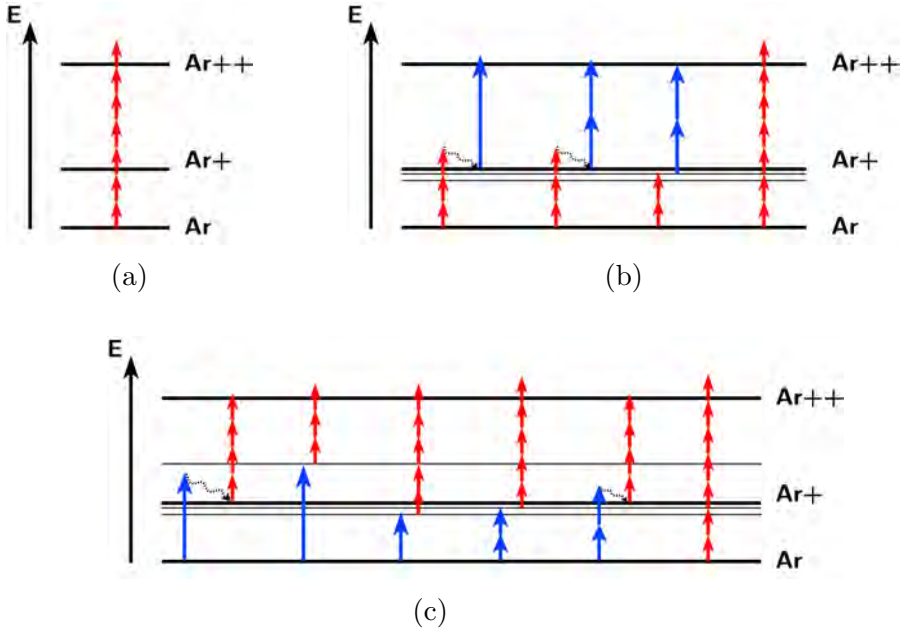

Figure 3.13: *Schematic presentation of all possible excitation paths. a) IR-only, b) IR-first, c) XUV-first*

Future experiments on this question should either record a detailed spectrum over the whole range of available wavelengths or, preferably, pick out only the desired part of the XUV spectrum and block everything else with a filter.

An Sn filter could precisely provide the desired XUV spectrum, with all transmitted harmonics exactly within the energy frame between the argon atom's ionization threshold of 15.8 eV and the argon ion's first excitation state of 29.4 eV. If an Sn filter were to be inserted into the beampath, the resulting spectrum would look like shown in figure 3.14. However, an Sn filter has the drawback that the IR would also be completely blocked.

As proposed by Ioannis Orfanos, this problem can be avoided by spatially separating the IR and the XUV beam. Only the beam closer to the xenon nozzle will encounter a high enough gas density to generate high harmonics. The polarization of both beams can be controlled individually so that when impinging on the silicon plate, the IR beam, which generated the XUV, is completely blocked while the second IR beam is partially reflected. The Sn filter is placed in the XUV beamline only, and both beams are recombined at

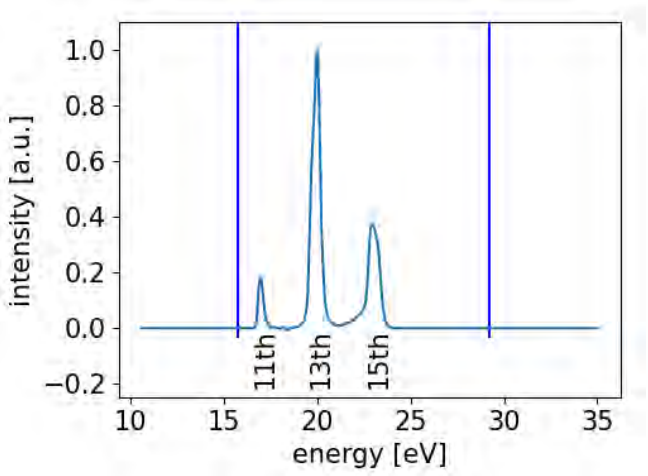

Figure 3.14: *XUV-spectrum when multiplying the final XUV spectrum of figure 3.12 with the transmission of an Sn filter. The left perpendicular line marks the ionization threshold of Ar, the right line denotes the first excitation state of* Ar^+.

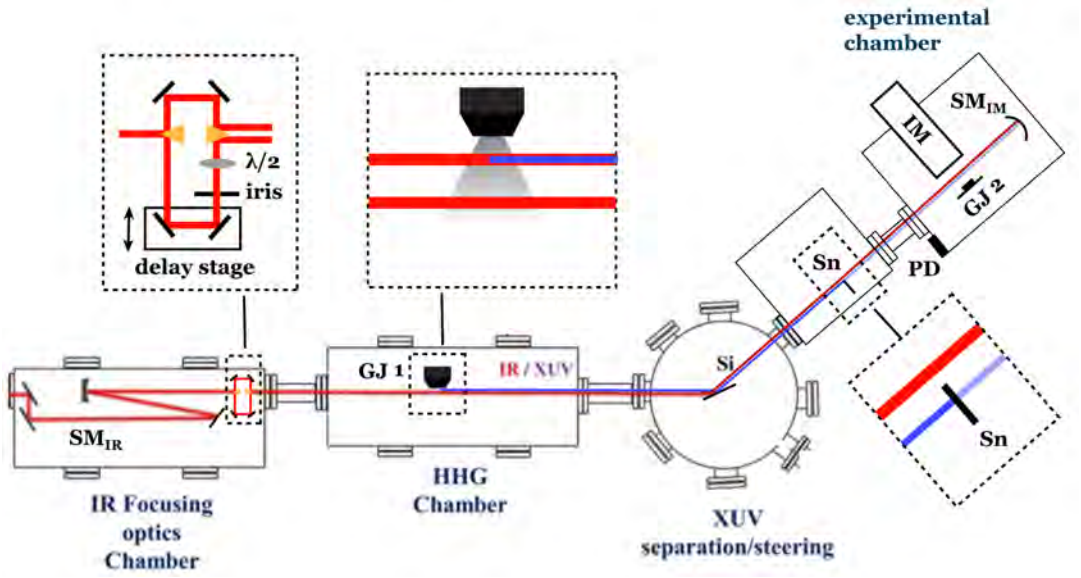

Figure 3.15: *Setup modified for spectral filtering.* SM_{IR}*: spherical mirror of* 9 m *focal length,* $\lambda/2$*: half-wave plate, GJ1: pulsed xenon jet, Si: silicon plate, Sn: tin filter,* SM_{IM}*: gold coated spherical mirror of* 15 cm *focal length, GJ2: Ar gas jet, IM: Ion microscope, PD: photodiode. Adapted from Nayak et al. [19].*

the focus in the IM. A possible modification of the existing setup including the filter is depicted in figure 3.15. The figure suggests gold prisms for beam separation. One could equally well use two beam splitters in combination with two additional mirrors.

Another argument in favor of the filtering setup is the facilitation of argon gas jet calibration. When observing a single photon process on argon, one can properly calibrate the argon gas jet density. Given the filtered XUV spectrum, Ar^+ is generated exclusively by a one-photon process and hence its spatial yield distribution does directly correspond to the gas density.

In general, such studies would be facilitated by an automatic determination of the correct voltages of the IM. This could save valuable time during the experimental campaign. The Differential Evolution algorithm presented in the course of the following chapter has the capability to do so in the sense of an autofocus for ion microscopy.

4.
Autofocus for Ion Microscopy

Since an ion distribution generated in a laser focus has hardly any outstanding features, it is difficult to determine during the experiment whether the image is blurred or not. As a consequence, the voltages applied to the electrodes are mainly determined via simulations. Corrections, which are necessary because of inaccuracy of the voltage sources and/or variations in laser pointing, remain rough. For this reason we propose automatizing the search for a suitable set of voltages, which results in a sharp image. A virtual grid is created by shifting the laser focus by a grid constant. The automatized search of the parameter space allows to include more parameters in the form of additional electrodes. Based on this idea we developed a novel IM design which we expect to be more versatile with respect to different magnifications. [9]

After presenting the newly developed generic IM design, the Differential Evolution Algorithm is introduced at first in general and later its application for the autofocusing of the IM is discussed. Then, the results of simulating the generic design are presented. The next section discusses a planned test run for the algorithm. The chapter closes with the considerations and steps made regarding the realization of a prototype of the novel IM at the Max Planck Institute of Quantum Optics (MPQ).

4.1 Setup

We simulate our generic IM using SIMION-8.1 [28], a software calculating electrostatic fields and ion trajectories for a given set of electrode voltages. The grid size used to model the geometry is set to 0.2 µm, since a further increase in resolution had no significant effect on the calculated ion trajectories. [9]

The final design features 23 electrodes including the repeller and extractor. We call our design the Generic Ion Microscope (GIM). Figure 4.1 illustrates the setup. An advantage of this generic design is the possibility to adapt different effective geometries. It can for example mimic einzel lenses at different positions

along the IM, depending on which electrodes are supplied with voltage and which are grounded. In contrast, simulating the physical shift of separate einzel lenses along the device would require a complete re-definition of the geometry passed on to the trajectory simulation program.

We found that it is sufficient if only the first 10 of these electrodes are considered for the optimization while the remaining electrodes are put to 0 V. This is discussed in more detail in section 4.4.1.

In comparison to other IMs, the inner diameter of our electrodes is relatively large. As a consequence, misalignments of the electrodes result in a smaller relative deviation and we expect aberrations due to misalignment to be less pronounced.

The setup was tested for its sensitivity towards the length of the vacuum tube, in the presented case 595 mm. It was found that length deviations of ±2 cm do not lead to a significant difference in the quality of the solutions found.

Also, a larger detector size of 60 mm diameter instead of 40 mm did not lead to a significant improvement in the obtained resolution.

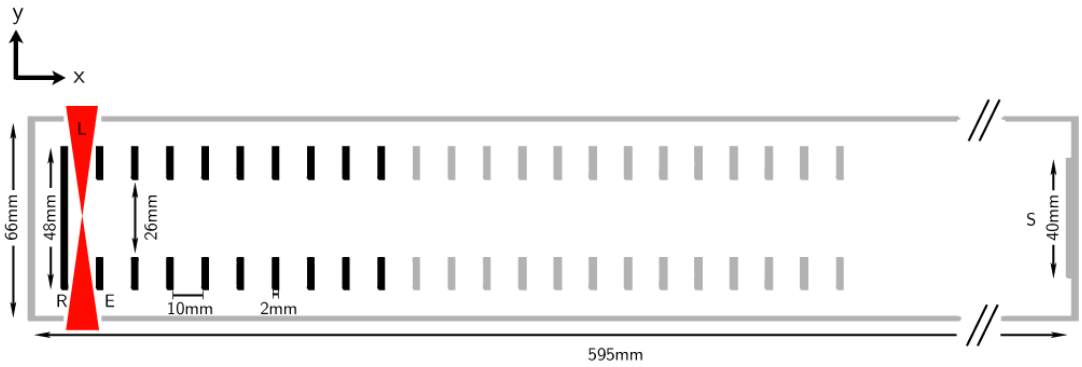

Figure 4.1: *Setup of the GIM featuring 23 electrodes, of which only the first 10 are active (black), the remaining ones are grounded (gray). The laser L passes between the repeller R and the extractor E. A screen S detects the generated ions.*

4.2 The Differential Evolution Algorithm

The evolutionary algorithm used to find the optimum electrode voltages belongs to a class of optimization algorithms called "Differential Evolution" (DE). Those kind of algorithms imitate nature's evolutionary process by randomly choosing members out of a given population, intermixing them to create so-called mutants

and finally keeping the best of the mutants and former population to form a new population. The process is repeated until some predefined ending condition is met.

More precisely, the starting population consists of N_{pop} members. Each member S represents one possible solution to the problem at hand in the form of a vector containing values for the N_{vars} variables to be optimized. In the beginning, those values are randomly chosen. The quality of each member is judged with a single quality factor L called "loss function". The way in which the loss function is calculated depends on the specific problem to be addressed.

As a next step, N_{mut} mutants are created. For this purpose three random members $S^{a,b,c}$ are chosen from the starting population and sorted by quality, so that solution a is the best of the three, c the worst. A new mutant vector M is then created as follows:

$$M = S^a + rand(1)\,(S^b - S^c). \tag{4.1}$$

$rand(1)$ indicates a number randomly sampled between 0 and 1. This ensures that in general the best of the three chosen solutions has the highest impact on the mutant.

During the exponential crossover process, a number k of successive vector components of a mutant M^i is kept with probability $(1-\alpha)\,\alpha^k$. All remaining values are directly inherited from the parent member S^i. We call $\alpha = 0.95$ the "crossover rate". Furthermore, there is the possibility to introduce small random mutations in the mutants' vector components. Finally, the values of a mutant are checked to be within the limits allowed for the respective variable $[v_{min}, v_{max}]$ and set equal to the respective boundary in case the limit is surpassed. The process of mutant creation is repeated until the desired number of mutants is reached. This results in a total number of solutions of $N_{pop} + N_{mut}$. All those solutions are sorted by quality and the best N_{pop} are kept as new population for the next generation.

A visualization of the process is given in figure 4.2.

The evolutionary process is finished if one of the following conditions is met: Either a predefined number of iterations N_{it} is reached, the quality of the best solution in the current population reaches a predefined goal L_{goal} or the algorithm converges. The algorithm is said to be converged if the relative difference between best and worst solution in a population is smaller than a given convergence limit L_{conv}: $L_{conv} < \frac{L^{(worst)} - L^{(best)}}{L^{(best)}}$. [9, 29]

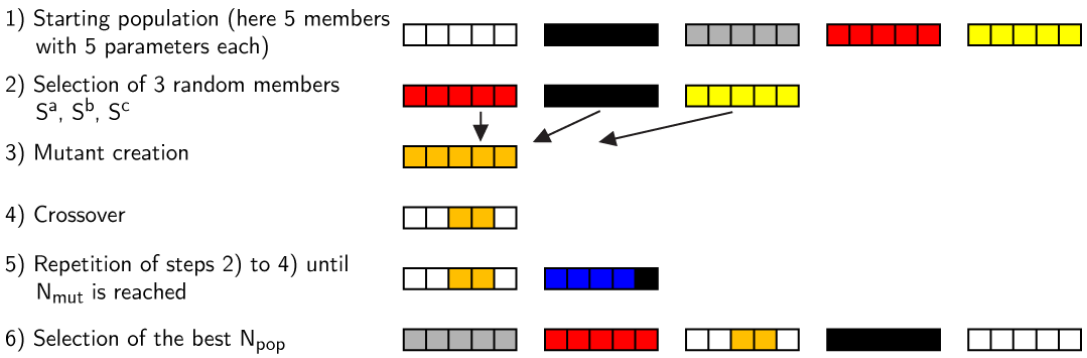

Figure 4.2: *Visualization of the optimization process.*

4.3 Implementation of the Differential Evolution Algorithm

Since it is nearly impossible to manually determine the voltages for all ten active electrodes of the IM setup presented in section 4.1, this task is instead performed by implementing the DE algorithm presented in the previous section 4.2.

In this case of ion microscopy, the population's members are 10-dimensional vectors containing the voltages for the 10 active electrodes, hence $N_{vars} = 10$. For the detection of positively charged ions, we want all electrode voltages to be positive or zero, the detector being set to 0 V. In case a value created by the mutant creation formula 4.1 turns out to be negative, the term in parenthesis is reversed for this specific value. Since this only prevents too small voltage values, additionally, the allowed parameter range is set to $[v_{min}, v_{max}] = [0\,\mathrm{V}, 10\,000\,\mathrm{V}]$, to confine the voltages on the high voltage side, as well. Larger maximum voltages of 15 kV and 20 kV were tested but didn't lead to a significant improvement in the resulting resolution. [9]

The population size is set to $N_{pop} = 20$, the number of mutants created in each generation evaluates to $N_{mut} = 10$ and no random mutations are applied.

The maximum number of iterations per run is set to $N_{it} = 50$, since most of the time the algorithm converges within 30 generations. To overcome the fact that the algorithm sometimes gets stuck in a local minimum or can't find a good starting point in the vast parameter space, usually three runs were conducted in a row while keeping the best solutions of the prior run as part of the starting population of the consecutive run. The solutions taken over to the consecutive run are dubbed "presets" and their number is determined by the *preset ratio*. It is usually set to 0.05. For a population size of 20, this corresponds to one inherited solution. It is also possible to include a preset solution already for the

first run of the algorithm, if a similar problem has already been solved by the algorithm, e.g. with a similar but slightly different magnification.

The criterion to be optimized is the resolution and the accuracy of the magnification. Since the initial ion position is not accessible in a real experiment, a realistic optimization procedure has to be performed with the entire ion distribution. To this end, we shift the laser focus to various predefined positions along a grid in the object plane. Because of the cylindrical symmetry, it is sufficient to move the focus position only to $N_{groups} = 3$ positions along the z-direction across the FOV. A number of $N_{groups} = 5$ positions has previously been tested as well but didn't show a significant improvement. A typical resulting image is depicted in figure 4.3, assuming a good voltage setting is already found and the image shows no notable aberrations.

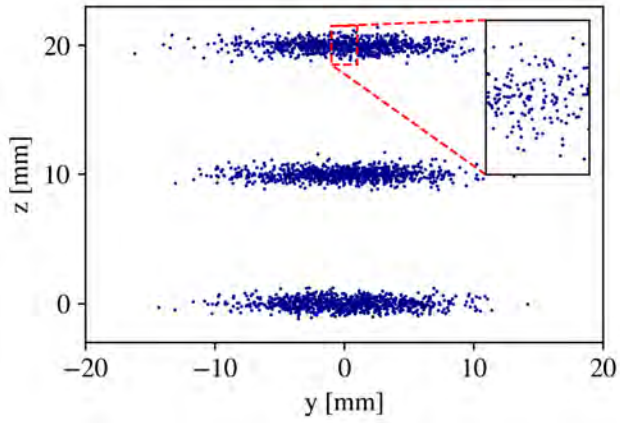

Figure 4.3: *Resulting effective grid by combining the images obtained from three focus positions shifted along the z-axis in one image. Image from Haniel et al. [9].*

The two shifted distributions are then compared with the initial unshifted one, taking into account the applied amount of shift and the nominal magnification. More specifically, we estimate the mean of the splat positions and their variance along the z-axis. From this, we determine three different quality criteria. The first one, $\Delta\mu$, is the absolute difference between the initial and the shifted beam's center coordinates in z after subtracting the applied shift times magnification. The second one is the difference $\Delta\sigma^2$ between the variances of the initial and the shifted ion distribution along z, and the third one is the variance σ^2 of the shifted ion distribution along z. Giving preference to small variances ensures that the optimum resolution is reached for the respective magnification. The resolution is mainly determined by how precise ions of the same starting position but with different initial velocity are depicted to the same point in the

image plane.

A visualization of those three parameters composing the loss function is given in figure 4.4.

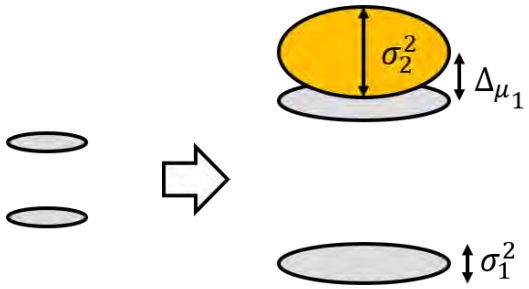

Figure 4.4: *Visualization of the entities evaluated by the loss function. Grey shapes on the left-hand side: Outline of focus at two positions in the object plane, grey shapes on the right: Outline of expected position in the image plane, orange shape on the right-hand side: Outline of an actual distribution suffering from aberrations.*

More concretely, for a magnification *mag* we choose the loss function

$$L = \frac{1}{N_{groups}} \sum_{i=1}^{N_{groups}} l_i \tag{4.2}$$

with

$$l_i = \begin{cases} \frac{w_1 \, |\Delta\mu_i|}{mag} + \frac{w_2 \, |\Delta\sigma_i^2|}{mag^2} \, (\frac{10\,\mu\text{m}}{FWHM_e})^2 + \frac{w_3 \, \sigma_i^2}{mag^2} \, (\frac{10\,\mu\text{m}}{FWHM_e})^2 & \text{if } M > 20 \\ w_1 + w_2 + w_3 & \text{else.} \end{cases} \tag{4.3}$$

with the expected ion beam width $FWHM_e$ and three weights w_1, w_2 and w_3 as further parameters. M denotes the number of particles out of the N ions started in the object plane which eventually reach the screen.

In case the number of particles hitting the detector is less than 20, the loss function is set to a large constant value. In an experiment, this would correspond to a significantly smaller number of detected ions than expected and would indicate that most ions hit some other part of the microscope than the detector.

The division by the magnification ensures that for solutions of the same quality with different target magnifications the resulting loss function value is the same.

The same kind of scaling has to take place with respect to the beam width by the factor $(\frac{10}{FWHM_e})^2$, as in reality, ion distribution FWHMs deviating from the simulated value of 10 µm are to be expected. Correspondingly, the expected beam width $FWHM_e$ has to be given in µm. This has the obvious drawback that one has to feed the algorithm an estimation of the expected ion distribution width. As a consequence, it is preferable to perform the autofocusing with a one-photon ionization process. In this case the ionization rate is proportional to the laser intensity and hence the FWHM of ion beam and laser beam are the same and can be easily estimated. Otherwise a conversion from laser FWHM to ion FWHM has to take place.

It should be noted that $FWHM_e$ is the only parameter requiring some prior knowledge about the ion distribution. Apart from that, all other parameters do not even require the ions to follow a Gaussian distribution. The mean and variance of the distribution are reliable criteria for the image's quality independent of the underlying distribution.

The relative weights of the different terms in the loss function were determined empirically via simulations to $w_1 = 2.5e3$, $w_2 = 1.5e5$ and $w_3 = 2.0e5$ and were found to yield a good balance between correct magnification and small variance as compared to other weight combinations investigated.

The loss function's performance is demonstrated in figure 4.5 where for a couple of solutions previously found by the algorithm, the corresponding resolution, deviation from desired magnification and attributed loss function value are plotted. The majority of solutions attributed with a loss function value of smaller than 6 have a resolution smaller than 2 µm. To be precise, the mean resolution is (1.8 ± 2.1) µm based on the evaluation of 25 solutions with a loss function smaller than 6. The resolution becomes (1.4 ± 0.5) µm if one exceptionally bad solution is neglected, which might be the result of a faulty data file. Based on this, the loss function value of $L_{goal} = 6$ was set as abort condition for the DE algorithm.

The third abort condition apart from the loss function goal of $L_{goal} = 6$ and maximum number of iterations of $N_{it} = 50$, is convergence. The convergence limit is set to $L_{conv} = 0.08$. However, abort due to convergence is only allowed if a loss function value lower than a certain threshold $L_{conv\ min}$ is reached. Otherwise a very bad starting population where the minimum ion number of 20 is not reached for any of the solutions will be judged converged, since the same large constant loss function value of $3 \cdot (w_1 + w_2 + w_3)$ is attributed to every population member. The consequence would be convergence after the first generation, which is not what we are looking for. [9]

An important point to be considered for the quality of the loss function is the precision in differentiating solutions of different quality with it. As one might

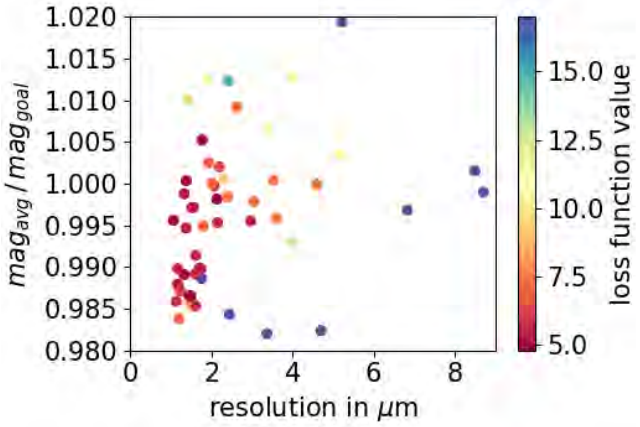

Figure 4.5: *Performance of the loss function in correlating a good coincidence with the desired magnification and a small resolution with a small loss function.*

already surmise from figure 4.5, the loss function range we are interested in is between 5 and 8. Solutions scored in this range have resolutions about 1 µm to 5 µm. As derived in the appendix section 7.2, the statistical error of the loss function, however, evaluates to 0.91, which covers about one third of the range of interest and prevents a more detailed resolution in the solutions' quality.

To reach a loss function precision of 0.5 in its current version, one already requires about 2700 ions. For the simulation, this would significantly increase the calculation time and is not feasible. For a real setup with a laser of repetition rate of 10 kHz, as available at the MPQ [30], even if only one ion is generated per shot, within one second 10000 ions are generated. The time of the optimization will not be bounded by the amount of generated ions anymore and the precision of the loss function can be increased significantly, considering that 10000 ions already correspond to an accuracy of 0.26.

Even though this is a drawback for the simulations, it is encouraging that in a real setup the reliability of the loss function's value attributed to a solution will significantly increase and allow for a credible discrimination between solutions' different quality graduations.

4.4 Simulations

To emulate an experimental ion distribution, we sample a three dimensional Gaussian ion distribution in the object plane with a width of $FWHM_{x,y,z} =$ 10 µm, 100 µm, 10 µm in the x, y, z-directions, respectively.

The simulated FWHM is realistic, since when assuming a Gaussian laser

beam with central laser wavelength of $\lambda = 750\,\text{nm}$, a mirror focal length of $f = 10\,\text{cm}$ and a beam FWHM at the focal mirror of $w_f = 0.2\,\text{cm}$, one obtains a minimum beam waist of

$$FWHM = \frac{f\,\lambda}{\pi\,w_f} = 12\,\mu\text{m}. \tag{4.4}$$

Schoetz et al. [30] report a beam waist of $< 10\,\mu\text{m}$ for the HORUS laser system, which is to be used for the future implementation.

The FWHM in y-direction doesn't directly influence the result of the algorithm. In the end, only the z-coordinate of a particle hitting the detector is evaluated. The criteria finally determining the simulated distribution width in y-direction were twofold. For one thing, the distribution should look like the elongated shape expected by a human analyzer and fill most of the FOV to display any aberrations, if present. Secondly, the width has to be small enough that the majority of the generated particles start within the FOV, even for the largest tested magnification of 100. Every particle starting outside the FOV will hit some other part of the IM than the detector. This just costs computation time and doesn't serve for the evaluation.

A point to keep in mind for the actual implementation is the need for compensation for a rotated image. The simulation always assumed the laser to be perfectly aligned with the y-axis and the shift to be performed exactly in z-direction. In reality this will not be the case. Most probably the recorded image has to be rotated by a few degrees before being fed to the analyzation algorithm. If not, the extracted distribution's FWHM will be larger than the actual value and the loss function's limits will not match anymore. However, this should be a minor issue, as for one specific setting, the rotation is expected to be always the same. It can be determined as soon as a first image is found, however poor the resolution might be.

The distribution is sampled with 800 ions for each focus position. In order to accelerate the convergence, we gradually increase the number of sampled ions up to 800 in the course of the optimization. The times for increasing the ion number are determined by the best solution of a population reaching a specific loss function value. [9]

Each of the sampled ions has an initial kinetic energy of 0.05 eV. This corresponds roughly to the expected mean thermal energy of $\overline{E_{kin}} = \frac{3}{2}\,k_B\,T = 0.04\,\text{eV}$ at a temperature of $T = 300\,\text{K}$. The kinetic energy gained from the laser field is negligible since we are interested in the heavy ionic cores. The spatial directions of the initial velocity vectors are random in all three dimensions.

4.4.1 Optimum Number of Active Electrodes

The initial setup considered for the GIM featured in total 23 electrodes in order to have a high flexibility. However, the larger the parameter space, the more difficult it becomes for the algorithm to converge towards the global minimum. Hence, a compromise for the size of the parameter space has to be found between a high versatility and fast convergence.

Haniel et al. [9] found this to be reached when only the first 16 electrodes are considered for the optimization. We call them the "active electrodes". The remaining electrodes are grounded and not considered for the optimization by the algorithm. Those electrodes are called "inactive electrodes". The result of 16 active electrodes was derived from a comparison of the number of solutions found within 1000 iterations for a magnification of 100 and 25, varying the number of active electrodes between 6 and 20. The optimization was conducted using a loss function with the known ion starting positions and without any preset solution in the starting population. For a magnification of 25, 16 electrodes reached the highest number of satisfactory solutions within 1000 iterations, while for a magnification of 100, 10 active electrodes would already be sufficient.

Based on this analysis, for this thesis the two settings with 10 and 16 active electrodes are analyzed in more detail. The target magnifications under investigation are once again 25 and 100. To emulate realistic conditions, instead of known ion positions, the loss function L analyzing the ion distribution is used and one preset solution is granted to the algorithm. The preset has a slightly different magnification, namely a magnification of 30 and 95, respectively, and the number of active electrodes corresponding to the setting under investigation. Then the optimization is independently started 20 times for each of the four settings (*mag* 100 and 10 electrodes, *mag* 100 and 16 electrodes, *mag* 25 and 10 electrodes, *mag* 25 and 16 electrodes). For each of the 20 optimizations, the algorithm is granted two runs, or in other words, is restarted once using the best solution of the first run as preset for the second run. The metric goal is switched off to see which setting gives the overall best solution.

Interestingly, the results shown in figure 4.6 lead to a different conclusion than Haniel et al. However, the two methods are not directly comparable, since different simulation conditions were applied, like for example the different loss functions.

Figure 4.6a shows that for a magnification of 100 and 16 active electrodes, even after just the first run of the algorithm, almost all solutions are below the threshold of a mean resolution over the FOV of 2 µm. When only 10 electrodes are considered for the optimization, more than 80% of the solutions still reach a resolution below 2.5 µm, only about 20%, however, reach 2 µm.

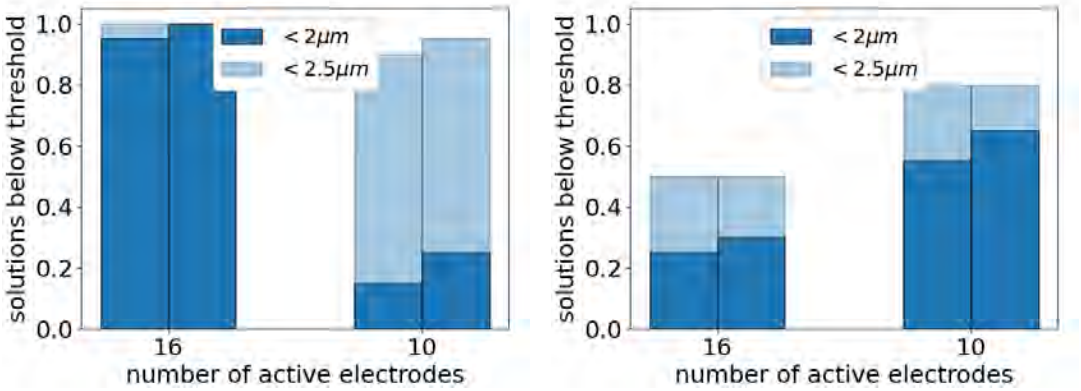

(a) *magnification 100x* (b) *magnification 25x*

Figure 4.6: *Portion of solutions with a mean resolution averaged over the FOV below* 2.5 µm *(light blue) and below* 2 µm *(dark blue) out of 20 optimizations for a target magnification of 100 (a) and 25 (b). For the two cases of 16 and 10 active electrodes, the result after the first run is plotted as the left column, the result after the second run as the left column, respectively.*

For a magnification of 25 and 16 active electrodes, 50% of the solutions are below the resolution of 2.5 µm. 30% of the solutions are below 2 µm after the second run of the algorithm. In the case of 10 active electrodes for the same magnification, however, 80% reach the threshold of 2.5 µm, 60% reach 2 µm. With respect to the absolute best solution found, no significant difference is observed between the four different settings.

Based on this, the number of 10 electrodes is judged sufficient for our goals and even beneficial in the case of small magnifications. Additionally, in terms of cost it is desirable to have a small number of active electrodes to reduce the number of voltage supplies necessary to operate the IM. For this reason, all further simulations as well as the final electrode design for the actual implementation use 10 active electrodes.

Once, tests have also been conducted to see whether the same imaging quality could be reached when the inactive electrodes were simply left out instead of being grounded. It turned out that the algorithm can also find comparably good solutions without the extra electrodes. But one cannot simply use a good solution obtained with grounded electrodes, remove the inactive electrodes and expect the solution to be of the same quality as before. The voltages have to be optimized for the new setup before a sharp image is obtained. This is reasonable, as the field free drift region is obtained without inactive electrodes as well,

since the surrounding vacuum vessel is grounded, but the decay of the fields is not equally fast for the two options with and without grounded electrodes.

4.4.2 Performance at Different Magnifications

The major outcome we wanted to achieve with the generic IM design was the resilience towards different magnifications.

To analyze this, we let the same DE algorithm optimize the electrode voltages of both our GIM and classical einzel lens microscope (ELM) for magnifications between 100 and 25 in steps of 5 towards the smaller magnifications. As a starting point, the algorithm is granted the solution of the next bigger magnification as part of the initial population. An exception is the starting magnification of 100, which gets a mediocre solution of the same magnification already previously found in other runs without preset. This procedure assumes that similar magnifications will probably have similar solutions. Without the preset the algorithm might get stuck far away from the optimum if all members of the initial population lead to poor results for example if all initial voltage sets create images where hardly any ions reach the screen. This is supposed to be prevented by restarting the algorithm several times, but the use of preset solutions significantly speeds up the process.

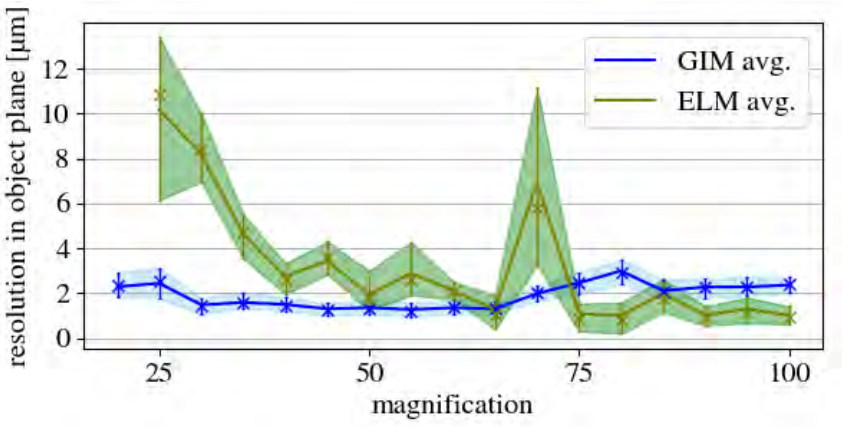

Figure 4.7: *Performance of the GIM and ELM at different magnifications when both optimized by the DE algorithm with the focus offset optimization described in section 4.3. Solid line and shaded area mark the average and variation of the resolution within the FOV, respectively.*

The results are put together in figure 4.7. The general trend holds that the GIM's resolution is pretty constant in its resolution while the resolution of the

ELM deteriorates towards smaller magnifications. One exception is the solution of magnification 60 of the ELM. Somewhat unfortunately it didn't manage to converge to a better solution within the allowed number of iterations. For magnifications larger than 75, the ELM performs better than the GIM with a resolution typically below 2 µm. The smaller the magnification becomes, the worse the ELM's resolution becomes up to a value of 13 µm at magnification 25, as one moves away from the magnification for which the einzel lens positions have been optimized. The GIM on the other hand has a mean resolution about 2 µm independent of the magnification and performs better than 3.5 µm in all simulated cases. As a consequence, with this device one can take advantage of a large FOV accompanied by a small magnification without suffering losses in the resolution.

4.4.3 Influence of Imprecise Focus Positioning

As the optimized voltages are always just determined for one specific x position of the object plane, we want to investigate the capability of the autofocus to adapt to different laser positions along the x direction, hence the principal axis of the IM. Additionally, the influence of the finite depth of the ion distribution is examined.

To this end, the optimization is run for three different positions of the object plane along the x axis with an offset of -0.5 mm, 0 mm and 0.5 mm with respect to the central position between repeller and extractor. The solution for offset 0 mm can be transferred directly from the magnification scan performed in the previous section without conducting a new optimization. The optimizations for an offset of ± 0.5 mm start with the solution of 0 mm offset as preset. The procedure is conducted for magnifications of 25 and 100 and for both devices, the ELM and the GIM.

The resulting solutions are analyzed with respect to their resolution along different x positions without further adaptations to the voltages and the findings are presented in figure 4.8.

The first result to be noted is that irrespective of the beam position in x direction, the algorithm is able to adapt the voltages accordingly to obtain a good resolution. This is valid for both tested magnifications and both devices. As a consequence for the experiment, if the image becomes blurred due to a slowly drifting beam position, one can simply re-run the autofocus to obtain a sharp image once again.

It is notable, however, that once the optimization has been conducted, the GIM is more sensitive to deviations of the object plane position than the ELM. The reason for that is most probably the relatively large inner diameter of

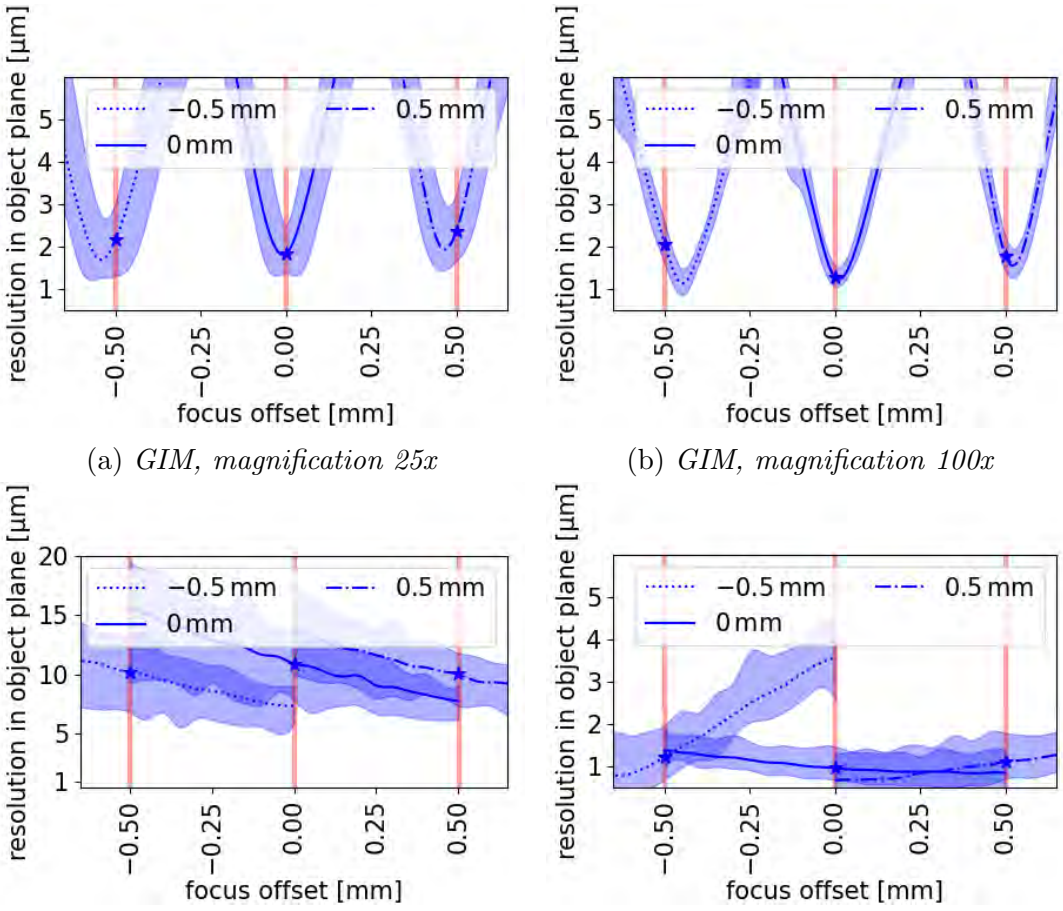

(a) *GIM, magnification 25x*

(b) *GIM, magnification 100x*

(c) *ELM, magnification 25x*

(d) *ELM, magnification 100x*

Figure 4.8: *Resolution within the FOV as function of the position of the object plane. Blue curves: Mean resolution within the FOV for pointing fluctuations. Blue shaded area: Range between minimum and maximum resolution within the FOV. Blue stars: Solution for a constant offset. Red shapes: Effect of the finite extent of an ion distribution with an FWHM of* 10 µm *on the resolution. Note that figure (c) has a different y-axis scale in comparison to the other subfigures.*

the GIM's electrodes. Reducing the inner diameter of the extractor to use it as intermediate aperture should increase the depth of field [31]. Nevertheless, within the width of the simulated ion distribution of 10 µm, the effect of the DOF dependence on the GIM's resolution is sufficiently small.

This leads us to the conclusion that irrespective of the magnification in the considered range and taking into account the ion distribution's finite width, even for the worst resolution within the FOV, we are able to reliably reach a resolution below 3.5 µm with the GIM.

4.4.4 Influence of Electrode Voltage Fluctuations

The final factor to be evaluated is the influence of fluctuations of the voltages applied to the electrodes.

Realistic voltage sources are not capable of perfectly accurately and repeatably setting a voltage. When told to set a specific voltage, there will be an offset between the desired value and the actual voltage applied by the power sources.

To determine whether and how this influences the solutions found by the DE algorithm, the simulation was manipulated in such a way that when the optimization algorithm dictated a specific voltage, the voltage actually applied to the SIMION electrodes deviated from this value by some random noise up to a maximum deviation voltage V_{dev}. The tested deviations are 100 V, 20 V, 10 V and 0 V. Their influence on the convergence is demonstrated in figure 4.9.

Fluctuations of up to 100 V clearly disturb the convergence and no satisfying solution could be found in all four optimization runs in figure 4.9a.

The effect becomes less pronounced for fluctuations of 20 V. Here it is worth looking at the resolutions obtained. The mean resolution achieved in the four runs averaged over the FOV is (3.0 ± 2.0) µm in the case of 20 V fluctuations. Deviations of 10 V on the other hand lead to a mean resolution of (1.3 ± 0.4) µm and show no notable difference to a simulation without voltage fluctuations resulting in a resolution of (1.36 ± 0.20) µm.

This desired voltage precision of 10 V corresponds to a realistic voltage setting reproducibility of 10 kV voltage sources, as specified by different manufacturers [32–34].

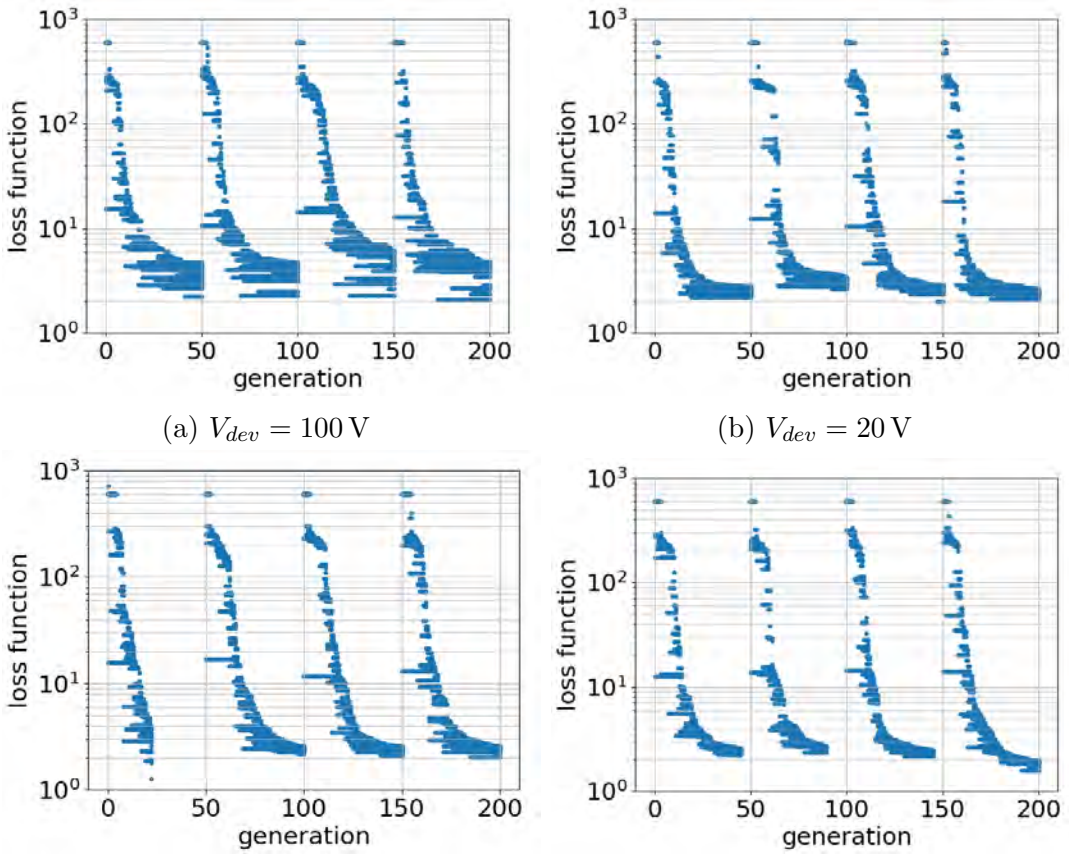

(a) $V_{dev} = 100\,\mathrm{V}$ (b) $V_{dev} = 20\,\mathrm{V}$

(c) $V_{dev} = 10\,\mathrm{V}$ (d) $V_{dev} = 0\,\mathrm{V}$

Figure 4.9: *Influence of deviations of up to V_{dev} in the electrode voltage on the convergence for a target magnification of 100. The optimization was started four times in a row with the same preset for all four runs in each plot. The loss function used for those optimizations was a former version and slightly altered to the presented one, so that the loss function's absolute values are different to the previously presented loss function. However, this doesn't influence the conclusions drawn from the figures.*

4.5 Test of the Autofocus on an Existing Ion Microscope

To test the feasibility of our autofocus, we planned running the algorithm on an existing IM. We chose the IMT12 by the Stefan Käsdorf GmbH [23], namely the exact same device at FORTH which has already been used for the experiments presented in section 3.

Setup of the IMT12

The setup of this einzel lens microscope is in principle very similar to the generic setup presented in figure 2.1. It consists of a repeller, an extractor and two einzel lenses. The extractor is also called "intermediate aperture". The detector is grounded. The detector consists of an MCP, a phosphor screen and, outside of the chamber, a CCD camera.

The four voltages applied to the repeller, extractor and the lenses are intended to be set manually via potentiometers. A view of the front panel is given in figure 4.10. The stigmators mentioned on the front panel allow for further aberration corrections but are not used in the experiments for this thesis. The IMT12 can detect both electrons and ions. In our case only the use as ion detector is of interest.

Figure 4.10: *Front panel of IMT12 showing the control potentiometers of repeller, extractor aka aperture, lens1 and lens2.*

Most of the information presented in this subsection is taken from the IMT12 manual [31].

Preliminary Considerations

The goal is to test whether the optimization presented in section 4.4 based on the shifted laser foci does indeed lead to a sharp image under realistic conditions.

If the initial population already contains a reasonable solution, the optimization typically takes about 15 generations until a sufficiently good solution is found. This translates to $(\#\text{generations} \cdot N_{mut} + N_{pop}) = (15 \cdot 10 + 20) = 170$ voltage settings to be tested. Even for a test run not intended for daily usage it is not feasible to do this manually. Hence, we have to automate the process.

To accomplish this task, the idea came up to connect four stepper motors to the four potentiometers. The next question is whether the achievable resolution is sufficient to reach the desired accuracy of 10 V. The decisive quantities to answer this are the turning angle of the potentiometer until it reaches the maximum voltage and the precision of the stepper's steps. Ten turns can be done until the potentiometer reaches its maximum value. This corresponds to a voltage of 10 kV. It has been confirmed that the transformation ratio, the number of turns of the knob divided by the corresponding number of turns of the axis, is 1. A typical stepper motor's resolution is an angle of 1.8°. Hence, the resolution is at least $\frac{10\,\text{kV}}{10 \cdot 360°} \cdot 1.8° = 5\,\text{V} < 10\,\text{V}$. This is sufficient for our optimization algorithm.

The test optimization is supposed to take about half an hour. To ensure this is feasible, the following paragraph will estimate the total time needed to set the voltages. Based on that, one can extract the minimum number of ions which have to be recorded per laser shot. If it were too many ions per shot, the resulting space charge would distort the image.

As a first step, we have to have a second look at the motor's step size. We drive our motors in quarter step mode, or in other words, we use four microsteps. This means that the actual mechanical step size of 1.8° is further broken down to $1.8°/4 = 0.45°$ by providing the voltages applied to the stepper's coils in the shape of a stepped sine wave rather than square pulses. The procedure is called *microstepping* and allows for a smoother rotation of the motor [35].

The stepper motors can be driven with an acceleration of $a = 16000\,\frac{steps}{s^2}$ and a speed of $24000\,\frac{steps}{s}$ as maximum allowed speed. The maximum speed is reached after 1.5 s of constant acceleration. Up to this time the motor has moved $\frac{1}{2}\,a\,t^2 = 18000$ steps, corresponding to 8100° or 22.5 turns. This is far more than the 10 turns of the potentiometer. As a consequence, for our case we can assume the movement to be continuously accelerated or decelerated, without a section of constant speed in between.

How much time does the motor hence need to make 10 turns? Since we are half of the time accelerating, half of the time decelerating with the same absolute acceleration value, we may calculate with an effective acceleration of $\frac{1}{2}\,a$. The desired angle $\alpha = 10°$ then relates to $\frac{1}{2}\,(\frac{1}{2}a)\,t^2$. Reorganizing the formula gives the time it takes to reach this angle: $t = \sqrt{\frac{4\,\alpha}{a}} = \sqrt{\frac{4 \cdot 10 \cdot 360°}{16000\,steps\,s^{-2} \cdot 1.8°/4}} = 1.4\,\text{s}$.

Accumulating the time the steppers need for the optimization gives $170 \cdot 1.4\,\mathrm{s} = 4.0\,\mathrm{min}$.

The time it takes the voltage sources to adapt to the new voltage setting is on the order of a few hundred ms, according to the manufacturer, and negligible.

Now we can calculate the minimum number of ions to be recorded per laser shot. To match with the simulations we require $N_{ions} = 800$ ions per image. To obtain the number of ions per shot we have to divide N_{ions} by the time per image and the laser repetition rate:

$$\text{ions per shot} = \frac{N_{ions}}{\text{time per image} \cdot \text{laser rep rate}}.$$

The latter one is read off directly from the laser parameters given in section 3.3 to be 10 Hz. The time available for taking one image is calculated as a fraction of the time allowed for the complete optimization t_{opt} by the number of images needed for the complete optimization N_{ims}:

$$\text{time per image} = \frac{t_{opt}}{N_{ims}}$$

Hence the resulting formula reads:

$$\begin{aligned}
\text{ions per shot} &= \frac{N_{ions} \cdot N_{ims}}{t_{opt} \cdot 10\,\mathrm{Hz}} \\
&= \frac{N_{ions} \cdot (N_{mut} \cdot N_{it} + N_{pop}) \cdot 3}{t_{opt} \cdot 10\,\mathrm{Hz}} \\
&= \frac{800 \cdot (10 \cdot 15 + 20) \cdot 3}{(30\,\mathrm{min} - 4\,\mathrm{min}) \cdot 10\,\mathrm{Hz}} \\
&= 26.2
\end{aligned}$$

We need to record at least 27 ions per image. For this ion number no space charge effects are to be expected.

Setup of the Test

To operate the steppers we for one thing need a corresponding driver and a connection between the axis of the steppers and the corresponding potentiometers.

When taking off the knob intended for manual potentiometer control, one can directly access the potentiometer's axis as seen in figure 4.11. With the use of an adapter the steppers can then be connected to the IMT12. To achieve some tolerance towards misalignment of the stepper's axis towards the potentiometer's axis both in angle and position, a double joint with flexible couplings together with an intermediate axis is planned, as depicted in figure 4.12.

Figure 4.11: *Potentiometer knob with and without cover.*

Mounting the motors at the correct heights in front of the IM's control panel requires some additional construction work. The flexible joints just allow for some small height differences on the order of a few millimeters. The motors' positions still have to roughly match the potentiometers' axes. To this end, we built some custom made mounts for the steppers, including some clearance allowing for final height and position adaptations on the setup. This mechanical setup is depicted in figure 4.13.

(a) (b)

Figure 4.12: *Double joint with intermediate axis straight (a) and bent to demonstrate the allowance for an axis offset (b).*

Steering a stepper requires a driver for taking care of applying the correct voltages to the stepper's coils. In this case we use four stepper motors of the type NEMA-17 in combination with DRV8825 drivers. The commands are transferred to the steppers via the drivers and an arduino microcontroller. The general wiring scheme is depicted in figure 4.14 and the resulting real circuit with all four motors connected is shown in figure 4.15.

A notable differences of the final setup to the schematic setup in figure 4.14 is that the schematic circuit drives the motor in half step mode. The degree of microstepping is controlled by different wiring of the driver. In figure 4.14 the

Figure 4.13: *Mechanical setup of the steppers.*

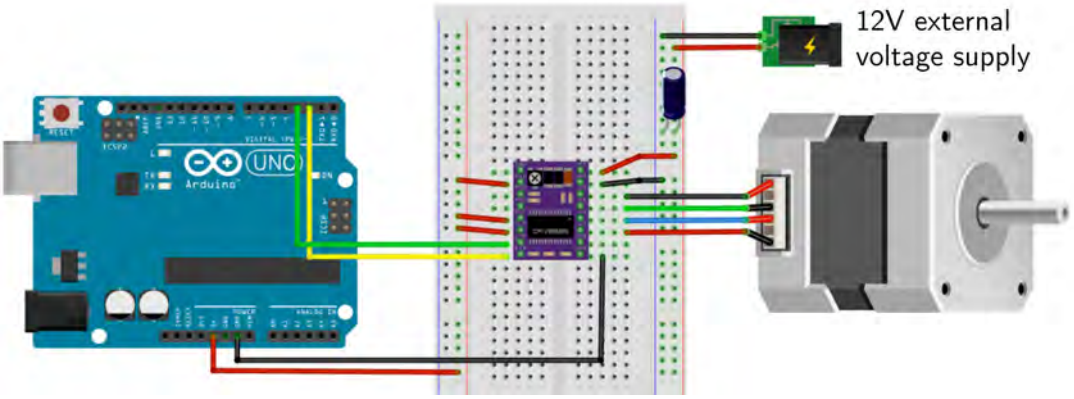

Figure 4.14: *Wiring principle of the circuit. Left: arduino board, center: wiring board with purple driver chip and black capacitor, right: voltage supply and stepper motor. [36]*

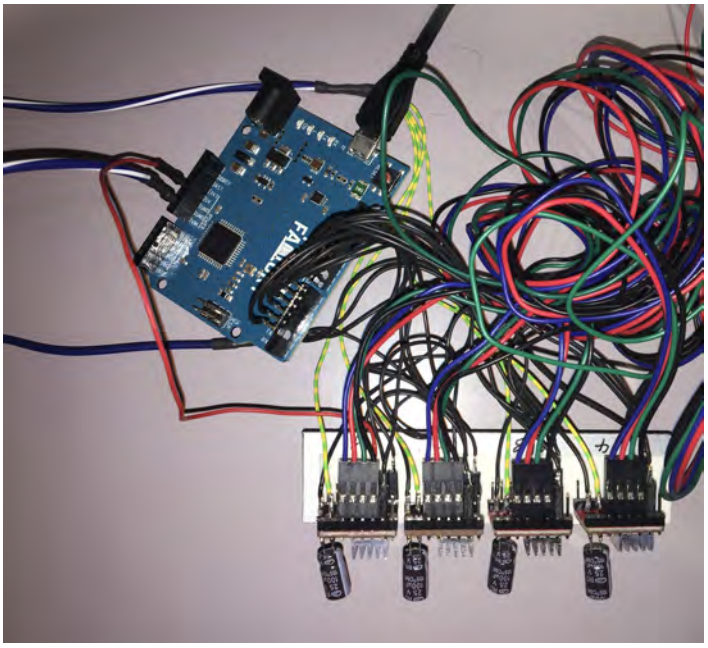

Figure 4.15: *Wiring of the real setup with all four drivers. The blue cables on the left of the image run towards the voltage supply, blue-white being connected to ground. The steppers are placed to the right of the image.*

red wires to the left of the driver are responsible for the microstepping. The setup in figure 4.15, however, uses quarter step mode.

A second difference between the two setups is the fault pin. If there is some fault, which hinders the driver to continue its operation, typically overheating, the fault pin is pulled down from the standard setting of 5 V to 0 V. In figure 4.14 this pin is not connected. It is the driver's second pin counted from the bottom right. For the final setup we did connect this pin to an input pin of the microcontroller and included its value into the program to warn the user in case of overheating.

The driver takes care of the actual voltage applied to the stepper to an extent that for starting the motor's movement, the user only needs to supply two binary input signals: *step* and *dir*, meaning whether or not to do a step and whether the turning direction should be positive or negative.

Onto the microcontroller we install the *AccelStepper.h* C++ library, which delivers an openly accessible and easy programming environment for accelerated stepper motor movements.

Those two components enable the user to do the final control via serial commands sent to the microcontroller. Such serial commands can be created by a python code and are for this reason easy to integrate into the existing

python optimization algorithm. The communication with the steppers has been successfully tested.

The mechanical and electrical construction work was mainly conducted by Christian Blank. For the mechanical setup we received further help from Frank Zeyer. Figure 4.16 gives an overview of the overall resulting stepper setup.

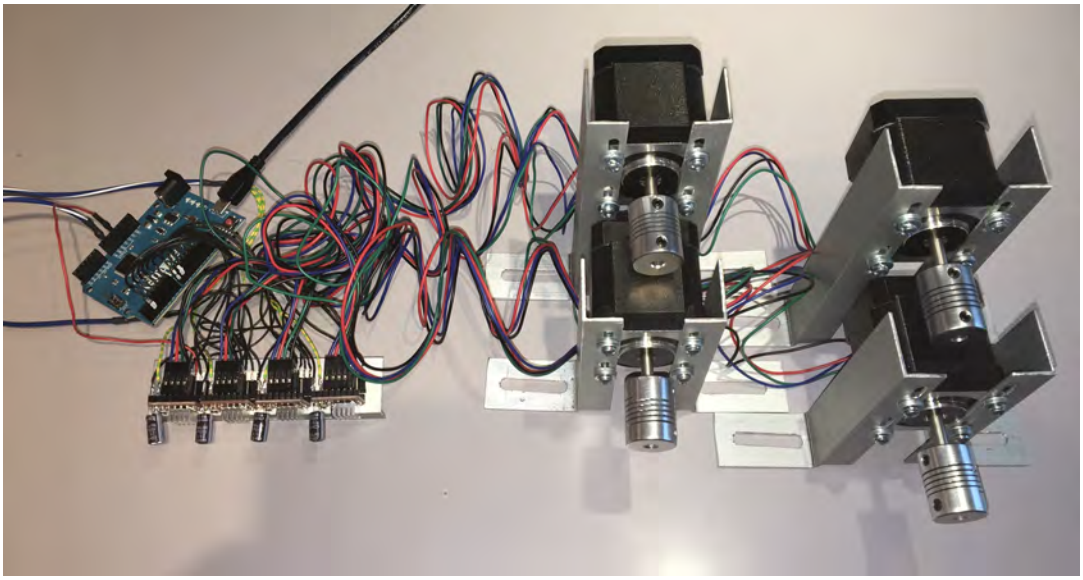

Figure 4.16: *Overview over the stepper setup.*

Connecting with the camera is more straightforward than the connection of the steppers. The model in use is an acA 1300 - 30um of the Basler AG [37]. The company directly provides a python library named *pypylon* for control of the camera including all relevant parameters like for example the integration time.

For successful execution of the experiment, all devices have to be controlled from one single program. A graphical user interface (GUI) depicted in figure 4.17 has been developed for simple control of all relevant parameters and steering of the respective devices. Before running the autofocus one should already have a reasonable IM image, which is to be further optimized. To obtain a first image, the GUI features a *voltage control* environment shown in figure 4.17a. A dummy image has been created as simulated camera feedback. One can track the current electrode's voltages and manually set specific voltages. An input window for the actual voltages indicated by the IMT12 front panel is necessary since the steppers cannot remember their absolute position and assume their starting position to be zero. Hence, one should always turn off the IM and the

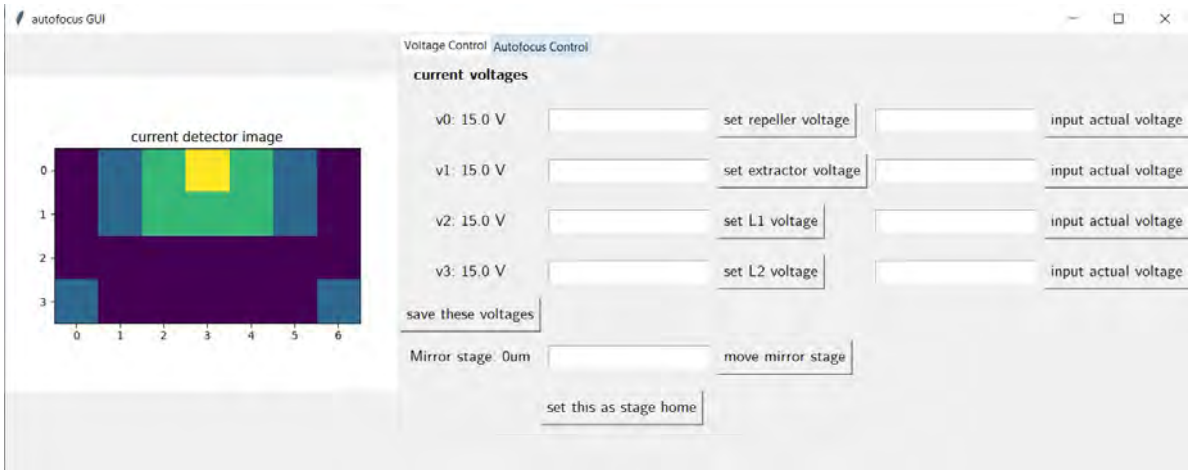

(a)

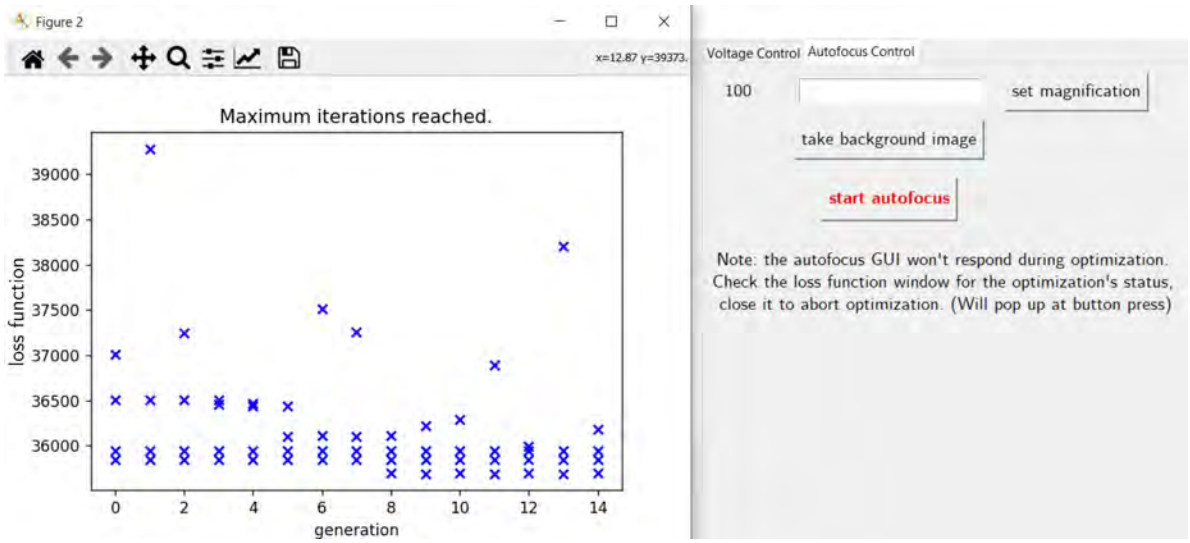

(b)

Figure 4.17: *GUI for the control of the autofocus via stepper motors, a CCD camera and a mirror translation stage featuring two tabs: voltage control (a) and autofocus control (b).*

steppers at an electrode voltage of zero. But for example unexpected electricity cuts or drifts after long periods of operation make it necessary to include this calibration option.

Once a reasonable setting is found, the voltages can be saved to be included into the starting population of the autofocus.

Additionally, the laser position can be adjusted via the mirror stage.

Switching to the autofocus control tab reduces the number of knobs to an input for the desired magnification, the possibility to take a background image and the starting button for the actual autofocus program. After starting the autofocus, an extra window shows the current status of the optimization in terms of loss function versus generation. For a real optimization this should resemble e.g. figure 4.9d. The image of figure 4.17b is the loss function based on the dummy image in 4.17a plus some random noise.

But before running the first try of an autofocus, a few calibration and test runs have to be conducted as explained in the following.

A crucial factor to the automatized voltage optimization is the repeatability of the voltages. The motors might miss a step from time to time. Accumulated, this might lead to an undesired offset between the voltage assumed by the motor control and the actual voltage. To ensure this doesn't influence our autofocus, one should attach a motor to the IMT12 and program the motor to continuously move from minimum to maximum voltage and back. This test program should run for a time longer than the autofocus, say for example for 45 min. The test is successfully passed if the voltage assumed by the program and the actual voltage do not deviate significantly.

Additionally one can confirm that the setting time of the voltage sources doesn't have to be taken into account. More precisely, one can measure the relation between camera reaction time and voltage setting time. This is done by taking an image directly after setting a voltage notably different to the current one and taking some images with a delay of a few hundred milli seconds. In case the images differ and hence the delay is notable, one has to force the autofocus algorithm to wait some time after setting a new voltage set until no difference is to be seen compared with the image obtained after a long waiting time.

Regardless of the previous efforts, the component which eventually forced us to give up on the test for the time being is the translation stage for the mirror. It is needed to translate the mirror in the course of the optimization. Control of the angle of the mirror is not necessary after the first alignment since, within first order approximation, for a spherical mirror a translational movement shifts the focus by the same amount. This is qualitatively demonstrated in figure 4.18.

For the same reason as with the voltages, it is not feasible to do this by hand.

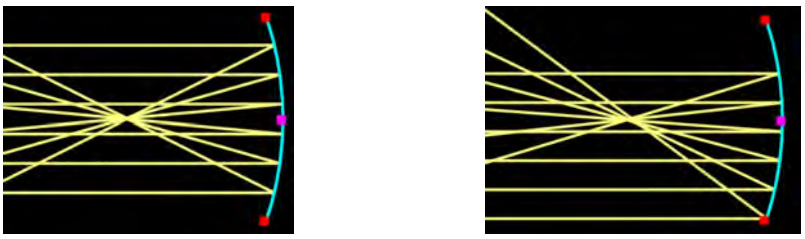

Figure 4.18: *Demonstration of the effect of translating a spherical mirror perpendicular to the incident laser. The simulation has been created with Ray Optics Simulator [38].*

As each voltage setting is tested with three different laser positions, the number of settings even triples for the mirror to $(15 \cdot 10 + 20) \cdot 3 = 510$. The mirror control used for the NSDI experiments was fully manual, so the translation stage had to be exchanged. The only vacuum compatible stage our colleagues at FORTH had at hand is a slip-stick drive. However, it is an open loop system, which doesn't give any feedback on its actual position. This alone would not be a problem if one could calculate back the position based on the starting position or if the error was negligibly small. Conveniently, the actual step size does stay constant for one specific motor as long as the load is constant. The problem is the different step size in the forward and backward direction. In the worst case, this difference is up to 100% of the step size, which is $\leq 30\,\text{nm}$ [39]. In our case, with at least 170 movements in the forward and backward direction (one laser scan per voltage setting), it is impossible to reach the necessary resolution of about 10 µm without a closed loop system.

The second approach of bringing a stage with us from Munich unfortunately failed since a satisfactory stage could not be found in time. The time window for execution of the experiment was already fixed since the autofocus test was supposed to run during the same visit at FORTH as the NSDI experiments presented in section 3. Ordering a new stage would have taken about 30 weeks.

Possible Improvements

In case the experiment will be conducted at a later point in time, there are a few things to be considered that might be improved with respect to the current version.

For one thing, the usage of servo motors might be more practical since those type of motors do remember their absolute position even after loss of power. Calibration would become easier in this case. Nevertheless, an option for calibration has to be kept, for example in case of drifts of the voltage sources over time.

It might be even better to re-design the experiment in a way that the potentiometers are not touched at all. Instead, one can take off the IMT12 front panel and directly access the output cables of the potentiometers. The potentiometers simply deliver an output voltage between 0 V and 10 V, which becomes amplified to the resulting high voltage. Instead of automatizing the potentiometer control, one can generate the corresponding low voltage control signal and put it onto the cables running towards the amplifier. [23]

It is also worth spending a thought on whether to migrate the control GUI to another programming language better suited for live control than python, like for example C++.

4.6 Implementation of the Generic Ion Microscope

To test the reliability of our so far only theoretical results, we started building an IM at the MPQ based on the simulations presented above.

The laser designated for testing the future prototype is a Ti:Sapphire system at MPQ with a central wavelength of 750 nm and a pulse duration of 4.5 fs in FHWM of the intensity envelope. Pulse energies up to 0.7 mJ are possible. [30, methods section]

The basis of the new IM consists of a vacuum chamber of a former velocity map imaging device shown in figure 4.19. The chamber includes a turbomolecular pump attached to it below the table. The laser will propagate along the y-axis on the height of the glass window seen in the lower part of the image. The detector will be mounted at the top of the chamber.

The glass window facing the observer on image 4.19 shall be replaced by a flange holding a spherical mirror on a translation stage inside the chamber. Placing the focusing mirror inside the chamber has the advantage of a more confined focus facilitated by a short focal length. The mirror's translation stage's movement has to be controllable in an automatized manner along the z axis for the optimization and be at least manually controllable along the x and y direction for beam alignment.

Detector

Regarding the detector, in principle, different options are possible.

Typically, IMs use a combination of an MCP, a phosphor screen, a glass window and a CCD camera for the signal detection. The disadvantage of this is the loss of the temporal information. The main reason for using an IM, in

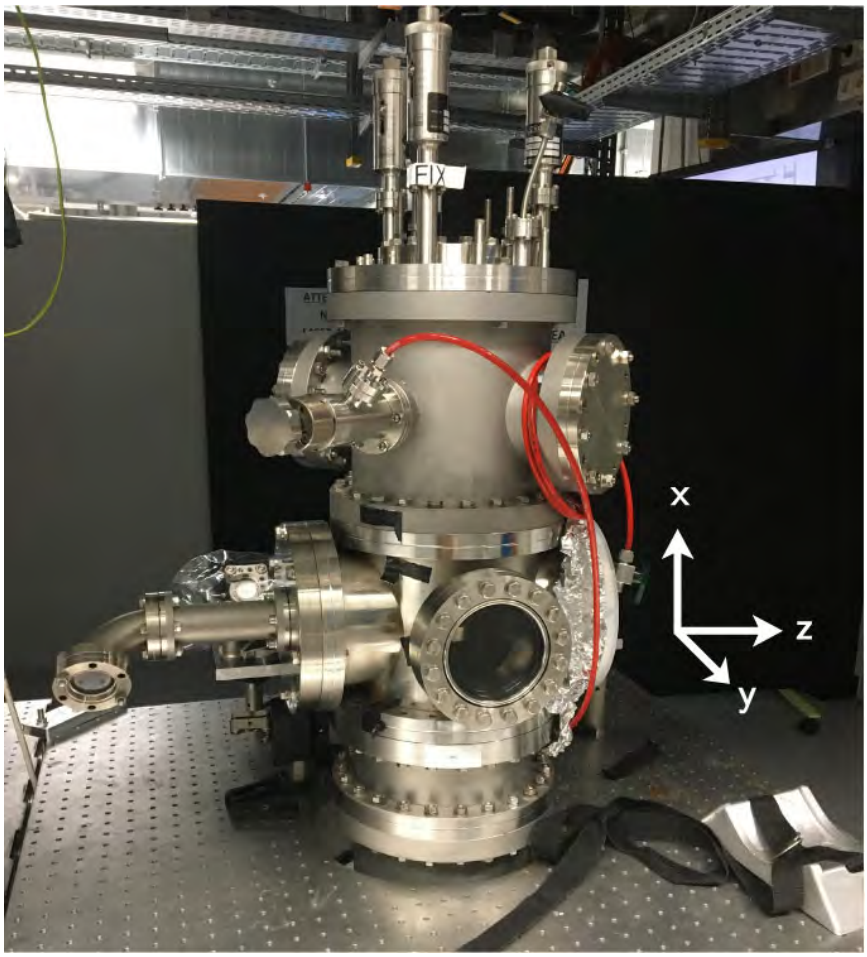

Figure 4.19: *Vacuum chamber of the former velocity map imaging device, which will serve as a basis for the future IM.*

contrast to a TOF, is the spatial resolution or, in other words, having the data in a not volume-integrated form. However, if the information about the exact splat timing is lost, one still averages over one dimension. In our notation this is the x axis.

For this reason, our preferred detector would have a temporal resolution on the order of 1 ns. Common CCD cameras cannot reach the required repetition rate. A fast up-to-date CCD camera system can for example be bought with a framerate of 200 frames per second, corresponding to a time resolution of 5ms [40]. Gating the MCP gives the possibility to obtain some temporal resolution. But this can normally only reach down to a magnitude of 50 ns, which is just sufficient to separate different ionic species but does not resolve features within the TOF peak of one species. Using special measures one can reach a gating pulse of 8 ns, which already allows for some temporal resolution [41]. However, all other information outside the gating window is lost. It would be desirable to have this temporal resolution as a standard feature of the detector system without the need for gating the detector.

To this end, a detection concept different from the CCD camera has to be used. In our case we already have a combined detector consisting of an MCP and a delay line anode available at the institute. The detector has an overall temporal resolution of < 0.2 ns [42]. A picture of it can be found in figure 4.20.

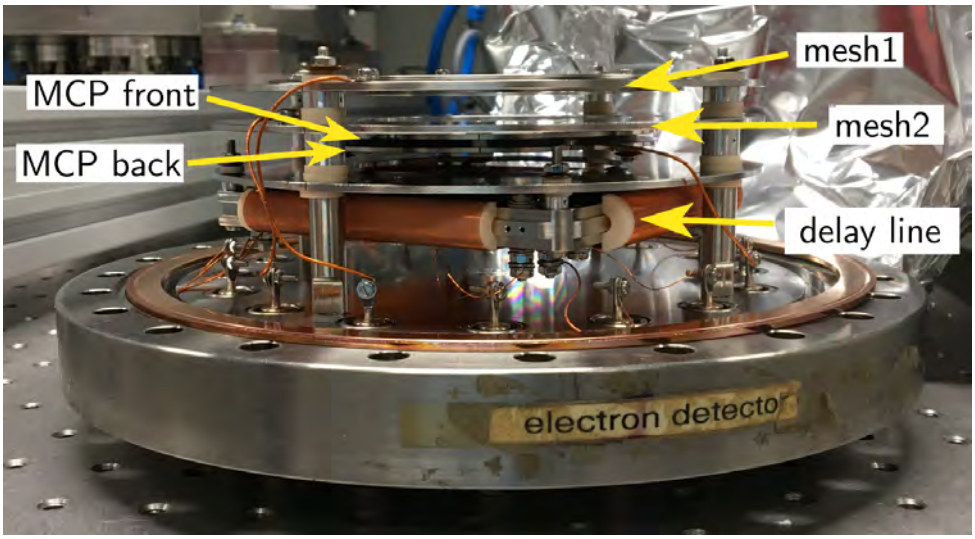

Figure 4.20: *Detector consisting of an MCP and a delay line. Annotations based on [43, figure A.2].*

The working principle of a delay line detector is the following: The detector itself is simply a plane spanned by a grid composed of two wires. One wire

is wound along the x axis, the second wire is wound perpendicular to the first one. If a charged particle hits the MCP, an avalanche of particles is generated. Particles which hit the MCP in between two channels can still be detected to some extent due to the two meshes in front of the MCP, which accelerate secondary electrons moving away from the MCP back towards the detector. The secondary electrons hit the two delay line wires and generate an electric pulse traveling along the wire. From the arrival time of the four pulses at the wire ends one can extract the splat position.

A significant disadvantage is that only very few particles can be detected within the time interval of signal travel. Otherwise the electrical pulses of one wire cannot be assigned properly to their respective counterparts generated on the second wire anymore, which is crucial for the determination of the splat position. By proper tuning of the laser intensity and target gas density one can ensure a sufficiently small event rate.

However, our preferred detection system would be not the delay line detector but another camera setup. Other camera concepts than classical CCDs can indeed reach the desired temporal resolution of about 1 ns, like for example the TPX3CAM by Amsterdam Scientific Instruments [44] with a resolution of 1.5 ns.

The next difficulty is finding a phosphor screen fast enough to satisfy this temporal precision. Even fast decaying P47 phosphor screens typically have a decay time of about 100 ns and for this reason cannot be used in this detector scheme [45, 46].

Fortunately, the TPX3CAM detection chip can detect both photons and electrons and withstand vacuum. Hence, one can place the chip directly behind the MCP in the vacuum chamber.

Regarding the fact that the delay line detector is already available at MPQ, in contrast to the TPX3CAM, our current plan is to use the delay line detector, even though it doesn't support high event rates per shot. At the same time, we want to keep an eye on opportunities for a setup with a fast camera.

Vacuum Conditions

Whichever detector we choose, all three considered options require an MCP. An MCP should be operated under vacuum conditions better than $2 \cdot 10^{-6}$ mbar [42]. Additionally, space charge effects are to be expected for pressures on the order of $\geq 3 \cdot 10^{-6}$ mbar [41].

Our GIM doesn't feature a gas jet as it has been used for the NSDI experiments of section 3. Instead, we plan to record the ions generated when homogeneously flooding the chamber with the target gas at low pressures.

A gas jet might decrease the chance to obtain an aberration free IM image. In case of a protruding gas nozzle, as used in the IMT12 experiments, the field lines between repeller and extractor become distorted. Repeller and extractor do not form a simple plate capacitor with homogeneous field lines anymore, which complicates the process of obtaining a sharp image. Admittedly, even without nozzle the setup is not an actual plate capacitor since the extractor has an annular shape. But including a protruding nozzle into the repeller introduces even more undesired complexity to the system.

Another possibility is to incorporate the nozzle into the repeller to obtain an even surface. In this case one still faces the challenge of an inhomogeneous gas distribution, which has to be considered and calibrated during data analyzation. For this reason it is preferable to record the signal from a homogeneous gas distribution, which has already been successfully done in other experiments [6].

In order to be able to distinguish the gas under investigation from other residual gases, the actual vacuum conditions have to be even better than the above mentioned $2 \cdot 10^{-6}$ mbar. Our target conditions are on the order of $1 \cdot 10^{-8}$ mbar. To introduce the low target gas pressures with a high precision, a needle valve is required.

All components of the GIM have to be compatible with those required ultra high vacuum conditions.

Electrodes

The electrodes were designed with the help of the MPQ technical team and manufactured by the MPQ technical workshop. The main task was finding a way to build the so far only schematic setup presented in figure 4.1. We ended up with a design based on four "rods" carrying the annular electrodes as depicted in figure 4.21. The rod setup is stable enough to support the electrodes and at the same time open-spaced to allow for reliable pumping.

In the first section containing the active electrodes, the rods are made from PEEK, a plastic compatible with ultra high vacuum. They are serving as insulator and mount at the same time. The rods carrying the inactive electrodes are made from steel. In this manner, all inactive electrodes can be grounded by the rods and the mounting, which are mechanically and hence also electrically connected to the grounded vacuum chamber, without the need for additional cables. The electrodes are fastened in their positions by inserting them into the notches along the rods.

The grounded electrode closest to the interaction region has a larger diameter. Apart from its purpose as electrode, it serves as a shield of the electric fields of the voltage-bearing electrodes towards the drifting area and stabilizes the setup. Additionally, the voltage-bearing cables are fixed at the rim of this

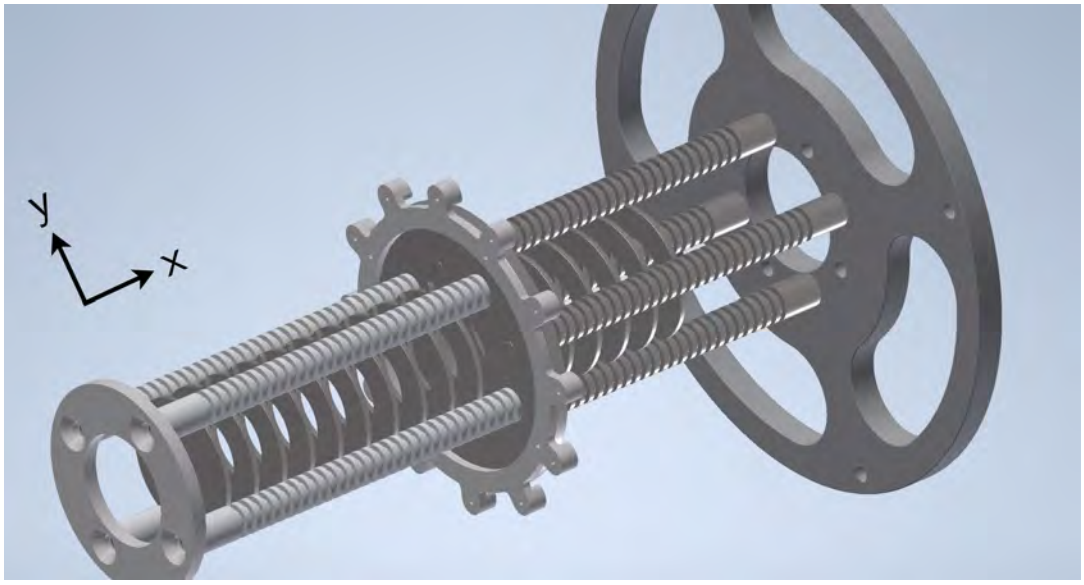

Figure 4.21: *Design of the future GIM's electrodes. Drawing by Tobias Kleinhenz.*

electrode. Fixing the cables at an intermediate position between their respective electrodes and the feed-through facilitates the task of keeping the necessary distance between the cables to avoid an electric breakdown.

Since the former VMI chamber is too short for placing the complete IM inside of it, an additional tube will be designed containing all the necessary cable feed-throughs. This tube will be inserted in the middle section between the target chamber and the upper part of the VMI chamber. The electrodes are fixed via the ring on the right-hand side of figure 4.21 at the transition between the central tube and upper tube. In the future, dismantling or updating the device can be easily accomplished by removing the upper tube and then either removing the central tube including the electrodes or directly taking the electrodes out of the chamber. A possible improvement of the setup might be for example the addition of field flattening electrodes behind the repeller carrying the same voltage as the repeller itself. An overview of the complete construction is given in figure 4.22.

A picture of the ready-made electrodes is presented in figure 4.23.

Voltage Sources

Finally, for the operation of the IM we need to apply the voltage determined by the algorithm to the electrodes. Each of the 10 active electrodes requires a voltage up to 10 kV, which has to be computer controllable and feature a repro-

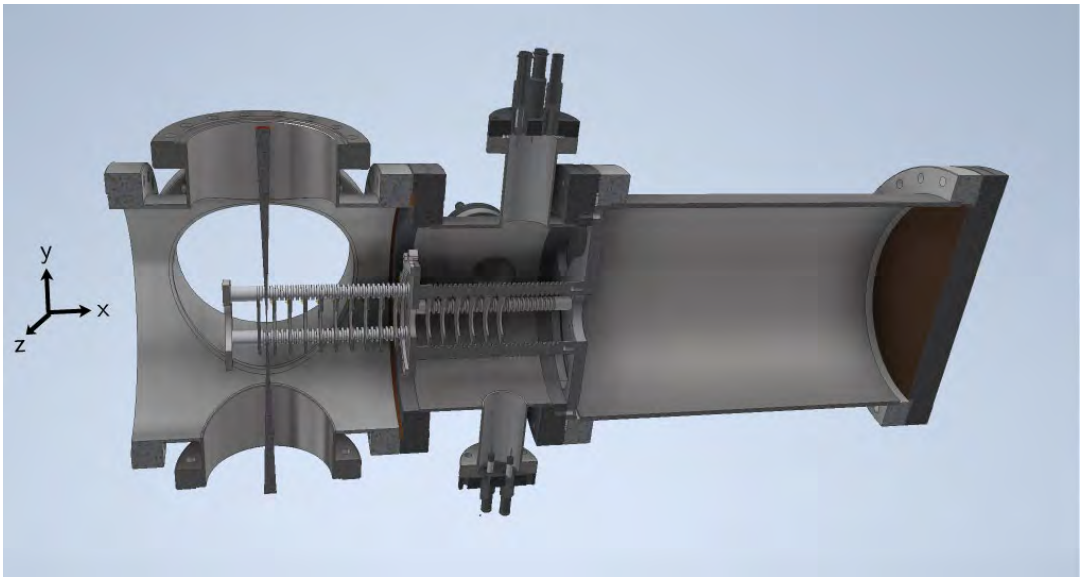

Figure 4.22: *Overview over the design of the future GIM. Drawing by Tobias Kleinhenz.*

Figure 4.23: *The GIM's electrodes manufactured by the MPQ workshop.*

ducibility of at least 10 V (cf. sections 4.4.1 and 4.4.4). Additionally, a fast voltage setting time is desirable on the order of 1 s. If the algorithm is supposed to converge within about 15 min, the setting time should not exceed 2 s. Assuming the algorithm needs 50 generations for convergence and the main contribution to the duration of the autofocus is the voltage-setting time, one obtains a runtime of $(\#\text{generations} \cdot N_{mut} + N_{pop}) \cdot \text{setting time} = (50 \cdot 10 + 20) \cdot 2\,\text{s} = 17\,\text{min}$ for a setting time of 2 s.

Since we hardly need any current, it is a reasonable idea to use one single voltage source, connect the electrodes in parallel and apply the required voltage to them via voltage dividers. However, for those high voltages no remote controllable voltage dividers exist. Digital potentiometers advertised as high voltage devices operate with an output voltage on the order of 10 V, far below the 10 kV necessary for our IM [47–49].

Instead, we plan to purchase 10 separate voltage sources. Possible suppliers providing sources with suitable specifications are for example FuG Elektronik GmbH [50], Heinzinger electronic GmbH [51] and iseg Spezialelektronik GmbH [52]. In what follows, their respective devices (available at the present time) fulfilling our requirements are presented in brief.

FuG offers devices of the type "HCE 35-12500 NEG". They feature a precision of $0.01\% \cdot V_{max} = 1\,\text{V}$ and a setting time at nominal load of $< 500\,\text{ms}$ for changes of the output voltage from 10% to 90% or 90% to 10% [34]. Our load is less than the nominal load, hence the setting time is expected to be even faster. Via a "Probus V interface USB MOD" module one can communicate with the devices using a USB cable and ASCII codes. Such ASCII commands can for example be generated by a python program.

Heinzinger suggests its "LNCE 20000 - 02" devices, featuring a precision of $0.1\% \cdot V_{max} = 10\,\text{V}$ and a setting time of up to 100 ms. This fast setting time can be reached if the high voltage is switched on and off every time the voltage is set to a new value, which can be done remotely. The voltage control is achieved via an analog signal between 0 V and 10 V. An additional digital to analog converter is necessary.

Iseg sells devices of the type "EHS 40 100p_S10". Their precision reaches $0.01\% \cdot V_{max} = 1\,\text{V}$ and the setting speed is up to $\frac{10\,\text{kV}}{0.2 \cdot V_{max}\,\text{s}^{-1}} = \frac{10\,\text{kV}}{2000\,\text{V}\,\text{s}^{-1}} = 5\,\text{s}$. Up to $0.75 \cdot V_{max}\,\text{s}^{-1}$ can be reached in principle, but in this case the voltage oscillates around the target value for the first few seconds with a magnitude of 100 V and the advantage of the fast setting time is lost. The device's controller can be addressed via python scripts.

Since all of the mentioned devices have the disadvantage of high cost and current delivery times on the order of several months, the actual implementation of the voltage supplies is beyond the scope of this thesis.

5.
Summary and Conclusion

In conclusion, the first part of this thesis presented an experiment investigating the generation of doubly charged argon ions via the strong field ionization of singly charged argon. Due to a sub-optimal XUV laser spectrum dedicated to prepare the target ions, we did not only generate the expected charge state, but most probably also a non-negligible contribution of other excited states of argon. This inhibited a clear conclusion from the obtained results. A modified setup circumventing this problem was proposed.

In the second part of the thesis, a novel generic IM design was presented along with the DE algorithm for the control of the voltages applied to the device's electrodes. The algorithm has the capability to automatically determine the correct parameters to obtain a sharp image, comparable to an autofocus. The novel IM has been tested for its performance with respect to different parameters. It has been demonstrated that for simulations of realistic conditions, resolutions below 3.5 µm can be reached in a large range of magnifications between 25 and 100.

Additionally, a test of the autofocusing algorithm on a real IM has been presented. The necessary components and programs have been discussed. In the end, the test could not be performed due to a missing component.

The final section treated the physical implementation of the generic IM design with a discussion of all its components. Some of the components are already implemented, others are pending. The presentation in this thesis shall give a robust basis for others to finalize the actual realization of the prototype.

For the future, it remains to be seen whether there is the possibility to conduct the experiment presented in the thesis' first part with the proposed corrections. This might give interesting insight into the nature of the ionization processes involved.

With respect to the generic IM, the presented design has the potential to simplify the research done with IMs due to its high flexibility with respect to the set magnification, while it doesn't show a notable loss in resolution.

Further improvements of the design can be investigated, for example by taking into account the electrodes' inner diameter or the electrodes' thickness for the optimization. Furthermore, the autofocusing algorithm can be applied not only to the presented IM but can in principle facilitate the operation of a broad range of imaging devices.

6.
Acknowledgements

While working on this thesis I received great support from numerous people. Although it is impossible to mention every person how directly or indirectly paved the way for this thesis, there are a number of people who I want to specifically thank at this point.

First of all I want to express my deep thanks to Boris Bergues for the supervision of my thesis and to Matthias Kling for the great opportunity to work in his group at LMU and later on mainly at MPQ.

Furthermore, this thesis wouldn't have been possible without the fruitful collaboration with Franz Haniel and Hartmut Schröder who set the foundations I based my work on together with Boris Bergues and all three of them kept working on the topic alongside me.

I want to express my sincere gratitude to our collaborators at FORTH for their warmest hospitality during my visits and the very rewarding experience of being part of the group of Paraskevas Tzallas. In particular, I had the pleasure of working together with Ioannis Orfanos, Ioannis Liontos and Manolis Skantzakis. Ευχαριστώ πολύ!

For valuable technical support my thanks go to Andreas Küchler, Harald Haas, Tobias Kleinhenz and the entire workshop crew at MPQ.

I want to thank Christian Blank for a great deal of mental and technical support and technical discussions, as well as his patience with me when talking about buggy algorithms he doesn't know.

Furthermore, I am very grateful to my proofreaders Franz Haniel, Guta Hedewig and Christopher McGahan.

Last, but not least I want to thank the whole Attoworld team and especially the Kling group for the supportive atmosphere where everyone I met was happy to lend a helping hand if needed.

7.
Appendix

7.1 Extraction of XUV Spectrum

For extraction of the XUV spectrum there are four different spectra available: one recorded with an indium filter, one with aluminum filter and a photoelectron spectrum with and without aluminum filter.

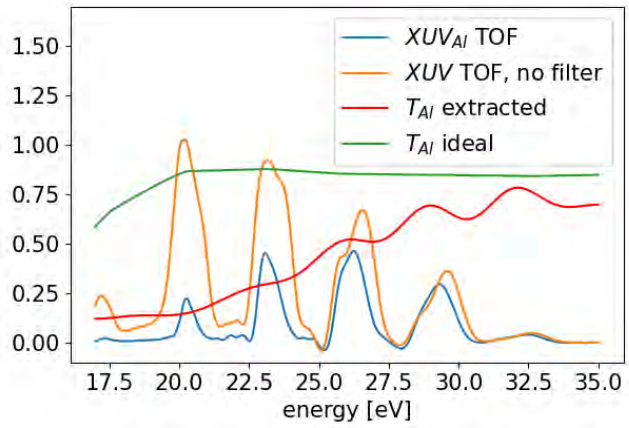

Figure 7.1: *Photoelectron spectra recorded with TOF and aluminum filter/no filter (XUV_{Al} TOF/XUV TOF, no filter) and the extracted aluminum filter transmission (T_{Al} extracted). T_{Al} ideal shows the transmission ideally expected for the aluminum filter [53].*

The photoelectron measurement in figure 7.1 with and without aluminum filter and the extracted transmission curve reveal that the actual transmission is quite different to the ideal one. This is caused most probably by degradation of the filter due to oxidation by air. The resulting Al_2O_3 surface layer modifies the transmission properties. The main change for the considered XUV spectral range due to oxidation is a reduced transmission for the lower energy side [54–56]. This fits well with the observed deviations from ideal filter transmission

seen in figure 7.1.

When working with the photoelectron spectrum one has to keep in mind that the spectrum is obtained by photoionization of argon. Hence the electron yields were multiplied with the photoabsorption cross section from Chan et al. [27] to yield the actual spectrum. Furthermore, the 11^{th} harmonic with 17.0 eV is just above the ionization threshold of argon of 15.7 eV. For this reason, the emitted photoelectrons have a very small kinetic energy and the detection efficiency of the TOF is reduced in this energy range. Only the 13^{th} and higher harmonics should be considered reliable when obtained from the photoelectron measurement.

As a consequence of the obvious aluminum filter degradations, we have to bear in mind possible deviations in the indium filter as well, even though there is no data available measuring the actual filter's transmission. Only the ideal transmission based on the data by Henke et al. [53] is available.

But indium hardly oxidizes with air at ambient temperature [57] and with age barely any absorptive surface layers emerge. It is mainly the manufacturing process and surface quality which play a crucial role in an indium filter's actual transmission. This will affect the overall transmission but typically not alter the relative transmission of different wavelengths. [56]

For this reason it was assumed that the indium transmission only has to be adapted by a constant prefactor with respect to the ideal curve. The factor is determined by matching the intensity of the 13^{th} harmonic obtained from the data recorded with the indium and aluminum filter.

The spectra recorded and corrected with indium filter and aluminum filter and the corresponding filter transmissions used for the eventual corrections are depicted in figure 7.2.

The resulting spectrum after overlaying the two spectral ranges obtained from In filter and Al filter still does not represent the spectrum present at the focus. Before hitting the argon jet, the beam gets reflected from a gold mirror. Its reflectance is calculated from the complex refractive index $(n + i\,k)$ determined by Werner et al. [58] available at NIST [26], using the following equation [21]:

$$R = \left| \frac{1 - (n + i\,k)}{1 + (n + i\,k)} \right|^2 . \tag{7.1}$$

Finally, the resulting reflectance and spectrum at target are presented in figure 7.3. The same spectrum can be found again in figure 3.12.

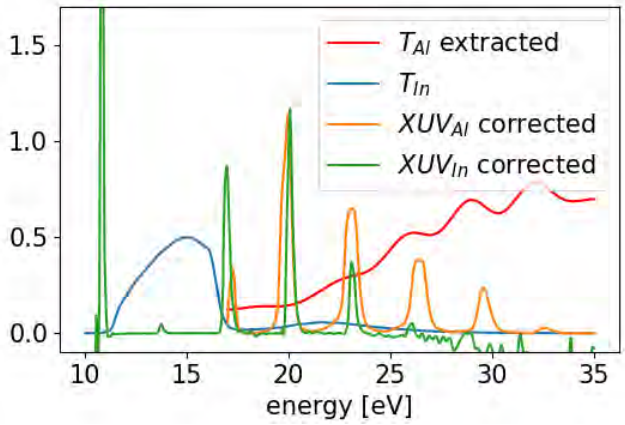

Figure 7.2: *XUV spectra recorded with aluminum filter and indium filter (XUV_{Al} corrected and XUV_{In} corrected) after correction by the worked out filter transmissions (T_{Al} extracted and T_{In}).*

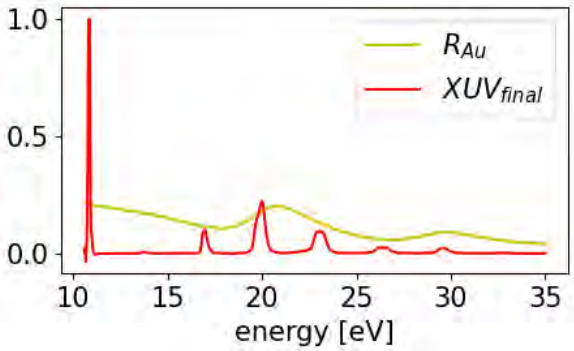

Figure 7.3: *Gold mirror reflectance R_{Au} and final XUV spectrum on target XUV_{final}.*

7.2 Statistical Error of the Loss Function

In the following lines, the statistical error of the loss function will be derived.

As a reminder, the loss function in a slightly modified way reads

$$L = \sum_{i=1}^{N_{groups}} w_1 \, |\overline{X}_i - \overline{X}_1| + w_2 \, |S_i^2 - S_1^2| + w_3 \, S_i^2.$$

For simplicity, and since we are just interested in the statistical error of sampling the ions in the object plane, we assume $mag = 1$, $FWHM_e = 10\,\mu m$ and $M > 20$. N_{groups} evaluates to 3, as in the whole thesis. The previous μ were replaced by $\overline{X}$ and σ by S. From now on we have to clearly differentiate between the mean μ and standard deviation σ of the actual underlying distribution and the measured values of the splats' mean $\overline{X}$ and standard deviation S. As a consequence, $\overline{X}_1$ and S_1^2 denote the mean position and variance of the splats resulting from the unshifted beam.

The error of the loss function is derived via propagation of uncertainties of its components.

The standard error of the mean for each of the beam positions $i \in \{1, 2, 3\}$ reads

$$\Delta\overline{X}_i = \Delta\overline{X} = \frac{\sigma}{\sqrt{N}}. \tag{7.2}$$

The error of the variance S^2 is calculated from a distribution's central moments μ_k [59, chapter 7]:

$$var(S_i^2) = \frac{\mu_4}{N} + \frac{3 - N}{N(N-1)} \, \mu_2^2. \tag{7.3}$$

For a Gaussian function we have the following central moments [60, chapters 4 and 6]:

$$\mu_2 = \sigma^2 \,, \;\; \mu_3 = 0 \,, \;\; \mu_4 = 3\,\sigma^4$$

Additionally, we make use of the relation

$$\sigma = \frac{FWHM_e}{2\sqrt{2\,\log(2)}}$$

After plugging in, we obtain for the error of the distribution's variance for all $i \in \{1, 2, 3\}$

$$var(S_i^2) = (\Delta S_i^2)^2 = (\Delta S^2)^2 = \frac{FWHM_e^4}{32\,\log(2)^2\,(n-1)}. \tag{7.4}$$

When plugging in the terms, it should be noted that the loss function value attributed to the unshifted beam position $i = 1$ consists only of $w_3\, S_1^2$, since the two subtractions evaluate to zero. Keeping this in mind, the error of the loss function becomes

$$\begin{aligned}\Delta L &= [\,(w_3\,\Delta S_1^2)^2 + \\ &\quad + \sum_{i=2}^{3} (w_1\,\Delta\overline{X}_i)^2 + (w_1\,\Delta\overline{X}_1)^2 + (w_2\,\Delta S_1^2)^2 + ((w_2+w_3)\,\Delta S_i^2)^2\,]^{\frac{1}{2}} \\ &= \sqrt{(w_3\,\Delta S^2)^2 + 4\,(w_1\,\Delta\overline{X})^2 + 2\,(w_2\,\Delta S^2)^2 + 2\,((w_2+w_3)\,\Delta S^2)^2} \\ &= 0.91\end{aligned} \tag{7.5}$$

This fits with the uncertainty observed for the loss function when evaluating the same solution several times.

7.3 List of Abbreviations and Physical Constants

c	$299\,792\,458\,\mathrm{m\,s^{-1}}$ (speed of light in vacuum)
π	3.141592654

DE	differential evolution
ELM	einzel lens ion microscope
FWHM	full width at half maximum
GIM	generic ion microscope
HHG	high harmonic generation
IM	ion microscope
IR	infrared (800 nm)
LMU	Ludwig-Maximilians-Universität München
MCP	microchannel plate
MPQ	Max Planck Institute of Quantum Optics
NSDI	non-sequential double ionization
TOF	time of flight
XUV	extreme ultraviolet

Bibliography

[1] P. B. Corkum and F. Krausz. «Attosecond Science.» In: *Nature Physics* 3 (2007). DOI: 10.1038/nphys620.

[2] C.J. Joachain, N.J. Kylstra, and R.M. Potvliege. *ATOMS IN INTENSE LASER FIELDS*. Cambridge University Press, 2012. ISBN: 978-0-521-79301-8.

[3] R. R. Jones. «Multiphoton Ionization Enhancement Using Two Phase-Coherent Laser Pulses.» In: *Physical Review Letters* 75.8 (1995), pp. 1491–1494. DOI: 10.1103/PhysRevLett.75.1491.

[4] P. Hansch, M. A. Walker, and L. D. Van Woerkom. «Spatially dependent multiphoton multiple ionization.» In: *Physical Review A* 54.4 (1996).

[5] B. Witzel et al. «Exact determination of spatially resolved ion concentrations in focused laser beams.» In: *International Journal of Mass Spectrometry and Ion Processes* 172 (1998).

[6] M. Schultze et al. «Spatially resolved measurement of ionization yields in the focus of an intense laser pulse.» In: *New Journal of Physics* 13 (2011). DOI: 10.1088/1367-2630/13/3/033001.

[7] P. Tzallas et al. «Time gated ion microscopy of light-atom interactions.» In: *Journal of Optics* 20 (2018). DOI: 10.1088/2040-8986/aaa326.

[8] B. Bergues et al. «Tabletop nonlinear optics in the 100-eV spectral region.» In: *Optica* 5.3 (2018), pp. 237–242. DOI: 10.1364/OPTICA.5.000237.

[9] F.E. Haniel et al. «Ion Microscopy with Machine-Learning Based Autofocusing.» (submitted).

[10] Thomas Dieterle. «An Ion Microscope for spatially resolved Rydberg Atom Detection.» MA thesis. 5. Physikalisches Institut, Pfaffenwaldring 57, 70569 Stuttgart: Universitaet Stuttgart, Nov. 2017.

[11] N. Tsatrafyllis et al. «The ion microscope as a tool for quantitative measurements in the extreme ultraviolet.» In: *Scientific Reports* 6 (2016). DOI: 10.1038/srep21556.

[12] Franz E Haniel et al. «Saturating multiple ionization in intense mid-infrared laser fields.» In: *New Journal of Physics* 23 (2021). DOI: 10.1088/1367-2630/abf583.

[13] A. L'Huillier et al. «Multiply Charged Ions Formed by Multiphoton Absorption Processes in the Continuum.» In: *Physical Review Letters* 48.26 (1982). DOI: 10.1103/PhysRevLett.48.1814.

[14] M. Kuebel et al. «Complete characterization of single-cycle double ionization of argon from the nonsequential to the sequential ionization regime.» In: *PHYSICAL REVIEW A* 93.5 (2016). DOI: 10.1103/PhysRevA.93.053422.

[15] Boris Bergues et al. «Single-Cycle Non-Sequential Double Ionization.» In: *IEEE Journal of Selected Topics in Quantum Electronics* 21.5 (2015). DOI: 10.1109/JSTQE.2015.2443976.

[16] B. Walker et al. «Precision measurement of strong field double ionization of helium.» In: *Physical Review Letters* 73.9 (1994).

[17] T. Schultz and M. Vrakking. *Attosecond and XUV physics : ultrafast dynamics and spectroscopy*. Wiley-VCH, 2014. ISBN: 9783527411245.

[18] J.B. Greenwood et al. «Suppression of Multiple Ionization of Atomic Ions in Intense Ultrafast Laser Pulses.» In: *Physical Review Letters* 88.23 (2002). DOI: 10.1103/PhysRevLett.88.233001.

[19] A. Nayak et al. «Multiple ionization of argon via multi-XUV-photon absorption induced by 20-GW high-order harmonic laser pulses.» In: *Physical Reviews A* 98 (2018). DOI: 10.1103/PhysRevA.98.023426.

[20] I. Makos et al. «A 10-gigawatt attosecond source for non-linear XUV optics and XUV-pump-XUV-probe studies.» In: *Scientific Reports* (2020). DOI: 10.1038/s41598-020-60331-9.

[21] W. Zinth and U. Zinth. *Optik - Lichtstrahlen, Wellen, Photonen*. 5th ed. De Gruyter Studium, 2018. ISBN: 978-3-11-049501-0.

[22] Refractive Index database. URL: https://refractiveindex.info/.

[23] Stefan Kaesdorf, Geräte für Forschung und Industrie, Gabelsbergerstr. 59 D-80333 München, Germany.

[24] N. Tsatrafyllis et al. «The ion microscope as a tool for quantitative measurements in the extreme ultraviolet.» In: *Scientific Reports* 6 (2016). DOI: 10.1038/srep21556.

[25] A. L'Huillier et al. «Multiply charged ions induced by multiphoton absorption in rare gases at 0.53 pm.» In: *Physical Review A* 27.5 (1983).

[26] A. Kramida et al. NIST Atomic Spectra Database (ver. 5.9), [Online]. Available: https://physics.nist.gov/asd [2022, July 11]. National Institute of Standards and Technology, Gaithersburg, MD. 2021.

[27] W.F. Chan et al. «Absolute optical oscillator strengths for the electronic excitation of atoms at high resolution. III. The photoabsorption of argon, krypton, and xenon.» In: *Physical Review A* 46.1 (1992), pp. 149–171.

[28] Scientific Instrument Services (SIS) by Adaptas Solutions, LLC. Adaptas Solutions, 9 Second Street, Palmer, MA 01069. USA. URL: https://simion.com/.

[29] Rainer Storn and Kenneth Prince. «Differential Evolution – A Simple and Efficient Heuristic for Global Optimization over Continuous Spaces.» In: *Journal of Global Optimization* 11.4 (1997), pp. 341 –359.

[30] Johannes Schötz et al. «The emergence of macroscopic currents in photoconductive sampling of optical fields.» In: *Nature Communications* 13 (2022). DOI: https://doi.org/10.1038/s41467-022-28412-7.

[31] Geräte für Forschung und Industrie Stefan Kaesdorf. *Manual - Ion Microscope IMT12*.

[32] Datasheet of PNC high voltage source by Heinzinger electronic GmbH. URL: https://www.heinzinger.de/fileadmin/user_upload/Datenblaetter/Katalogseiten/DE/Universal-Hochspannungs-Netzgeraet-PNC-heinzinger-catalog.pdf.

[33] Datasheet of EHS high voltage source by iseg Spezialelektronik GmbH. URL: https://iseg-hv.com/files/media/iseg_datasheet_EHS_en_20210607111806.pdf.

[34] Datasheet of HCP high voltage source by FuG Eletronik GmbH. URL: https://www.fug-elektronik.de/wp-content/uploads/pdf/Datasheets/EN/HCP_data_sheet.pdf.

[35] URL: https://www.motioncontroltips.com/faq-what-is-microstepping/.

[36] Tutorial on controlling a stepper motor with DRV8825 driver. Accessed 26.07.22. URL: https://starthardware.org/stepper-motor-mit-dem-drv8825-steuern/.

[37] Basler AG, An der Strusbek 60-62, 22926 Ahrensburg. Accessed 25.07.2022. URL: https://www.baslerweb.com/en/.

[38] Yi-Ting Tu and Wei-Fang Sun. *Ray Optics Simulation*. URL: https://ricktu288.github.io/ray-optics/.

[39] Article on *Open vs. Closed Loop Picomotor Control* by Newport Spectra-Physics GmbH, accessed 22.07.2022. URL: https://www.newport.com/n/open-vs-closed-loop-picomotor.

[40] Fast Frame Rate CCD Scientific Camera for Microscopy by Thorlabs Inc. Accessed 20.07.2022. URL: https://www.thorlabs.de/newgrouppage9.cfm?objectgroup_id=7485.

[41] Alexander Muschet. «Characterization of intensive attosecond XUV pulses.» Master thesis. Ludwig-Maximilians-Universität München, 2015.

[42] Manual of the delay line detector by RoentDek Handels GmbH, accessed 20.07.2022. URL: file:///C:/Users/Hedewig/Desktop/Autofokus/implementation/literature%20-%20implementation/MCP%20Delay%20Line%20manual%20-%20RoentDek.pdf.

[43] Nora G. Kling. «Controlling the Dynamics of Electrons and Nuclei in Ultrafast Strong Laser Fields.» PhD thesis. Kansas State University, 2013.

[44] TPX3CAM by Amsterdam Scientific Instruments, Science Park 106, 1098XG, Amsterdam, The Netherlands. Accessed 20.07.2022. URL: https://www.amscins.com/tpx3cam/.

[45] Phosphor screens by ProxiVision GmbH, accessed 20.07.2022. URL: https://www.proxivision.de/wp-content/uploads/PV_Phosphor_Screens_201601.pdf.

[46] Phosphor Screens by Lambert Instruments BV, Leonard Springerlaan 19, 9727KB Groningen, The Netherlands, accessed 20.07.2022. URL: https://www.lambertinstruments.com/phosphors.

[47] Datasheet on the high voltage digital potentiometer AD7376 by Analog Devices, Inc., accessed 31.08.2022. URL: https://www.analog.com/media/en/technical-documentation/data-sheets/AD7376.pdf.

[48] Datasheet on the high voltage digital potentiometer DS3502 by Maxim Integrated, Inc., accessed 31.08.2022. URL: https://datasheets.maximintegrated.com/en/ds/DS3502.pdf.

[49] Datasheet on the high voltage digital potentiometer CAT5133 by Semiconductor Components Industries, LLC, accessed 31.08.2022. URL: https://www.onsemi.com/pdf/datasheet/cat5133-d.pdf.

[50] FuG Elektronik GmbH, Am Eschengrund 11, 83135 Schechen, Germany. URL: https://www.fug-elektronik.de/.

[51] Heinzinger electronic GmbH, Anton-Jakob-Strasse 4, D - 83026 Rosenheim, Germany. URL: https://www.heinzinger.de/.

[52] iseg Spezialelektronik GmbH, Bautzner Landstr. 23, 01454 Radeberg, Germany. URL: https://iseg-hv.com/en.

[53] B.L. Henke, E.M. Gullikson, and J.C. Davis. «X-Ray Interactions: Photoabsorption, Scattering, Transmission, and Reflection at E = 50-30,000 eV, Z = 1-92.» In: *Atomic Data and Nuclear Data Tables* 54 (1993). Accessed via the corresponding online database. DOI: 10.1006/adnd.1993.1013. URL: https://henke.lbl.gov/optical_constants/.

[54] Jiri Schmidt et al. «Long-term changes in Al thin-film extreme ultraviolet filters.» In: *Applied Optics* 60.28 (2021). DOI: 10.1364/AO.432592.

[55] Masatoshi Hatayama et al. «High-Transmittance Free-Standing Aluminum Extreme Ultraviolet Filter.» In: *Japanese Journal of Applied Physics* 48 (2009). DOI: 10.1143/JJAP.48.122202.

[56] W.R. Hunter and R. Tousey. «Transmittance of thin films in the extreme ultraviolet.» In: *Le Journal de Physique* (1964). DOI: 10.1051/jphys:01964002501-2014800.

[57] Harry Schoeller and Junghyun Cho. «Oxidation and reduction behavior of pure indium.» In: *Journal of Materials Research* 24 (2008). DOI: 10.1557/JMR.2009.0040.

[58] Wolfgang S.M. Werner, Kathrin Glantschnig, and Claudia Ambrosch-Draxl. «Optical Constants and Inelastic Electron-Scattering Data for 17 Elemental Metals.» In: *Journal of physical and chemical reference data* 38.4 (2009), pp. 1013–1092.

[59] V.K. Rohatgi and A.K.E Saleh. *An introduction to probability and statistics*. John Wiley & Sons, 2015. ISBN: 9781118799642.

[60] Arak M. Mathai and Hans J. Haubold. *Probability and statistics: a course for physicists and engineers*. De Gruyter, 2018. ISBN: 9783110562545. DOI: 10.1515/9783110562545.

Selbstständigkeitserklärung

Hiermit erkläre ich, die vorliegende Arbeit selbständig verfasst zu haben und keine anderen als die in der Arbeit angegebenen Quellen und Hilfsmittel benutzt zu haben.